Impact of the local microstructure fluctuations on radiation-induced segregation in dilute Fe-Ni and Ni-Ti model alloys: a combined modeling and experimental analysis

Liangzhao Huang, Kan Ma, Lisa Thinhinane Belkacemi, Marie Loyer-Prost, Estelle Meslin, Elin Toijer, Luca Messina, Christophe Domain, Julien Vidal, Maylise Nastar

Impact of the local microstructure fluctuations on radiation-induced segregation in dilute Fe-Ni and Ni-Ti model alloys: A combined modeling and experimental analysis

Liangzhao Huang[a,*], Kan Ma[a,*], Lisa T. Belkacemi[a,*], Marie Loyer-Prost[a], Estelle Meslin[a], Elin Toijer[b], Luca Messina[c], Christophe Domain[d], Julien Vidal[d], Maylise Nastar[a]

[a] *Université Paris-Saclay, CEA, Service de Recherches de Métallurgie Physique, 91191, Gif-sur-Yvette, France*
[b] *KTH Royal Institute of Technology, Nuclear Engineering, SE-114 21 Stockholm, Sweden*
[c] *CEA, DEs, IRESNE, DEC-Service d'Études et de Simulation du Comportement des Combustibles, Cadarache F-13108 Saint-Paul-Lez-Durance, France*
[d] *EDF R&D, Department of Materials and Mechanics of Components, F-77250 Moret sur Loing, France*

Abstract

From a systematic atom probe tomography (APT) characterization of the radiation-induced segregation (RIS) in dilute Fe-Ni and Ni-Ti model alloys, we highlight fluctuations of the solute local concentration up to the scale of the APT specimens. We deduce the RIS at dislocation loops from a solute diffusion equation, that is solved at steady state, within the Voronoi's volume occupied by a single loop. From a statistical sampling of the Voronoi's volume and the dislocation loop radius modeled after the characterization of the microstructure by transmission electron microscopy, we provide the full RIS distribution. The present statistical approach of RIS demonstrates that the fluctuation of local solute concentrations in Fe-Ni and Ni-Ti mainly results from the dispersion in size and density of the dislocation loop population. Besides, we highlight the impact of the post-treatment parameters used in the APT protocol on the extracted RIS profiles. In Ni-Ti alloys, the simulated Ti-depletion profiles are in very good agreement with the measured ones. Furthermore, the dispersion of the loop radius and density is shown to play a critical role on the fluctuations of the Ti local concentration. In Fe-Ni, the identification of discrepancies between the simulated Ni-enrichment profiles and the measured ones provides a signature of additional operating mechanisms of the solute redistribution, such as radiation-induced precipitation.

1. Introduction

Irradiation creates Frenkel pairs made up of a vacancy and a self-interstitial atom (SIA). These point defects (PDs) diffuse and eliminate at structural defects acting as PD sinks such as dislocation lines, dislocation loops and voids. Due to solute-PD interactions in alloys, the net fluxes of PDs make solute atoms diffuse towards or away from the structural defects, inducing a change of the alloy composition close to the PD sinks. This phenomenon is the so-called radiation induced segregation (RIS) [1, 2, 3, 4, 5]. Stationary RIS is reached when back diffusion of solute at sink balances the solute composition change resulting from the solute-PD flux couplings. Although not often mentioned, a by-product of RIS is the redistribution of solute atoms away from the sinks [3, 6].

The variation of the alloy composition near the structural defects resulting from RIS may induce the material's failure [7, 8]. For example, chromium depletion at grain boundaries was suggested to be responsible for the decrease of the corrosion resistance in austenitic steels [9], and phosphorus enrichment at grain boundaries results in material embrittlement [10]. The redistribution of solutes far from sinks, by triggering phase transformations, may be a destabilizing factor of the matrix [3]. Besides, RIS may affect the adsorption bias of a PD sink between vacancies and SIAs, thereby have an impact on the swelling behavior of the material. There is increasing evidence that radiation-induced precipitation phenomena start with RIS, suggesting that RIS may be a precursor of precipitation. In case precipitation goes with a change of long-range order, a diffraction technique may provide a direct evidence of the transition between RIS and precipitation, as for instance the precipitation of the Ni_3-Si ordered phase in austenitic steels [2, 11]. In case of bulk precipitation phenomena, RIS at dislocation loops is suspected to be the main precursor. In situ investigations have shown that the α' precipitation in Fe-Cr alloys occurs on radiation-induced dislocation loops [12]. There are indirect evidences of a RIS-to-RIP transition at dislocation loops. They mainly rely on the characterization of the microstructure evolution with the radiation dose. An

*Corresponding authors

Email addresses: `huang.liangzhao@outlook.com` (Liangzhao Huang), `k.ma@bham.ac.uk` (Kan Ma), `belkacemi@iwt-bremen.de` (Lisa T. Belkacemi), `maylise.nastar@cea.fr` (Maylise Nastar)

early-dose RIS of solutes at dislocation loops, a late-dose observation of Mn-Ni-Si-rich precipitates in RPV ferritic steels [13, 14, 15], as well as Ni-rich austenitic phases in an ion-irradiated Fe-3%Ni model alloy [16] suggest that the precipitation starts from RIS at dislocation loops. Note that, in these systems, precipitates seating on dislocation loops were not found, as if the removal of the dislocation loop was a necessary step of the phase transformation [17].

Most of RIS characterizations have been performed on grain boundaries. RIS behaviors of various materials, for various initial microstructures, and at various irradiation conditions have been thoroughly studied in industrial materials (e.g., refs. [18, 19, 5]), but a lot less in model alloys [3, 5]. In irradiated materials, we commonly observe non-uniform densities and large-size distributions of dislocation loops [20, 21]. RIS, as well, varies from one sink to another. Currently, there is no systematic study of the effect of the microstructure dispersion in size and density on RIS behaviors.

In this work, we focus on the relationship between RIS and the local microstructure properties. The investigated materials are chosen to be the body-centered cubic (bcc) dilute Fe-Ni and the face-centered cubic (fcc) dilute Ni-Ti model alloys. The Fe-Ni and Ni-Ti model alloys are of interest to the nuclear industry because they constitute model alloys of respectively the current reactor pressure vessel steels and the advanced austenitic steels that are considered for future nuclear systems [22]. In these materials, Ti is added to prevent swelling [22]. Note that a full characterization of the microstructure and RIS in Fe-Ni irradiated at high radiation flux [23] and at low flux, with light [24] and heavy particles [16] have been published. In these samples, in low-fluence regions, dislocation loops are systematically enriched in Ni. At higher fluences, dislocation loops were replaced by fcc precipitates [16, 17]. Here, we provide a systematic characterization of the Ni segregation at dislocation loops in the same model alloy, but exposed at higher radiation flux. In the case of Ni-Ti alloys, RIS is poorly known. Auger electron spectroscopy showed the oversized Ti atoms to be segregated away from the surface of the foil, between 400 and 650 °C, whereas at temperatures near 25 °C, Ti segregated to the surface [3]. A recent *ab initio* study shows a crossover temperature of 320 K (47 °C) above which RIS of Ti is negative, in line with the experimental observations [25]. Besides, Ti has a strong impact on the radiation-induced microstructure. Under self-ion irradiation at $T = 450$ °C, SIAs agglomerate as single or multi-layer extrinsic Frank loops and vacancies into voids, while, in pure Ni, vacancies agglomerate into intrinsic Frank loops and SIAs into inner intrinsic Frank loops [21]. Among the questions left in both materials, are the impact of (i) the nature of the dislocation loop on RIS, (ii) the heterogeneity and distribution in size of the loop population on the amplitude of RIS.

Ab initio calculations of the PD energetic properties, including the PD-solute binding energies and PD migration energies, when combined with a diffusion calculation method [26, 27], are able to predict the sign of RIS, at least in dilute metallic alloys [28, 29, 30, 31, 25]. Recent simulations relying on a combined *ab initio*–KineCluE–rate theory method have provided a quantitative modeling of RIS at perfect planar sinks in Fe-based dilute alloys, with respect to the alloy composition, the irradiation conditions, and an average sink strength of the microstructure [32]. However, elastic long range interactions between sinks and PDs, that were ignored in this study, may strongly affect RIS. For instance, we may have a change of sign of RIS between the tensile and the compressive regions of the dislocation loop, or a greater amount of the overall RIS when compared to RIS at surface or a wide-angle grain-boundary (due to a stronger interaction with the lattice PDs). Only a few modeling studies have investigated the impact of the elastic interactions on PD-solute flux couplings [33, 34], and the resulting RIS [35, 36]. These RIS simulations were performed for an edge dislocation line, and the effect of strain on the non-conservative character of PDs [37] was missing. The elastic interactions of a dislocation loop strongly vary with its size [38]. Besides, it has been shown that the radius of loop and the local distribution of the dislocation loops described by a Voronoi distribution, are key control parameters of the PDs fluxes [39]. Therefore, we expect that the size and spatial dispersion of the dislocation loop population leads to non-uniform RIS from one dislocation loop to another.

As an important step towards a full understanding of RIS and its relationship with the local microstructure, we present a combined modeling and experimental study of the RIS dispersion in Fe-Ni and Ni-Ti dilute alloys. By relying on the published *ab initio* diffusion database and performing *ab initio* calculations of the PD and solute elastic dipoles with respect to their local environment, we calculate the solute-PD flux couplings by means of the KineCluE code [27] based on the self-consistent mean field diffusion theory [40, 41]. These strain and composition-dependent flux couplings are input parameters of the diffusion equation to be solved within the Voronoi volume of the dislocation loop. To reproduce the main properties of the microstructure characterized by Transmission Electron Microscopy (TEM), we introduce then a statistical modeling of the radius and Voronoi volume of the dislocation loop, in order to reproduce the main properties of the microstructure characterized by Transmission Electron Microscopy (TEM). Impact of the microstructure dispersion on RIS will be investigated in details. For the comparison with direct Atom Probe Tomography (APT) analysis of the solute redistribution at dislocation loops and away from them, we will emphasize the role of the number and the volume of the APT specimens on the results, and provide criteria on the representativeness of the experimental data in Fe-Ni and Ni-Ti.

This paper is organized as follows: Section 2 is devoted to a short presentation of the experimental methods, including the sample preparation, the irradiation conditions, and the analysis methods. In Section 3, we present the

diffusion model and the numerical setup to simulate the RIS profiles. Then in Section 4, we introduce the modeling method of the dislocation loop microstructure. The TEM characterization of the microstructure and the APT analysis of RIS and the solute redistribution away from the dislocations can be found in Section 5 and Section 6, respectively. The simulated RIS profiles, as well as a parametric study of RIS with respect to the local microstructure features, are presented in Section 7. In Section 8, we compare the simulated RIS profiles to the experimental ones, then we discuss the differences between the two alloys, the limitations of the model, and eventually suggestions for improvement for future RIS studies. A summary, concluding remarks, and perspectives are given in Section 9.

2. Experimental procedure

2.1. Studied model alloys

Two high purity samples were studied: Ni-0.48at.%Ti and Fe-3.3at.%Ni. They will be referred as Ni-Ti and Fe-Ni respectively. Both were manufactured by cold crucible induction melting at Ecole des Mines de Saint-Etienne (EMSE, France). The measured impurities in Ni-Ti and Fe-Ni are in mass ppm (O $\leq$ 14, C $\leq$ 2, N $\leq$ 1, S $\leq$ 4) and (O $\leq$ 35, C $\leq$ 23, N $\leq$ 4, S $\leq$ 4) respectively. Slices of Ni-Ti were cut and mechanically polished to 70 µm thick. Disks of with a diameter of 3 mm were punched out and annealed at 1273 K for 2 hours in a vacuum of 10^{-7} mbar followed by air-cooling. Annealed samples were electro-polished in a methanol-nitric acid solution on one side. Fe-Ni alloy was annealed before the cutting. It underwent an austenitization annealing, a cold reduction and a recrystallization thermal treatment at 1173 K for 16 hours under pure Argon flow. It was then cut and mechanically polished to 100 µm thick. 3 mm diameter discs were punched out from the 10 mm diameter discs and electropolished in methanol-perchloric acid solution on one side to remove the superficial hardened layer.

2.2. Irradiation conditions

The irradiation of the two model alloys of interest was performed at the JANNuS-Saclay facility. The irradiation conditions are different for these two alloys.

- Fe-Ni is subjected to 2 MeV Fe^{3+} ion irradiation, at 400 °C, at a flux of 8.6±2.2 × 10^{11} ions·cm^{-2}·s^{-1} up to a fluence of 2.1±0.5 × 10^{15} ions·cm^{-2}.

- Ni-Ti is irradiated by 5 MeV Ni^{2+} ions, at 450 °C, at a flux of 2.1±0.5 × 10^{11} ions·cm^{-2}·s^{-1} up to a fluence of 2.3±0.5 × 10^{15} ions·cm^{-2}.

Dose and ion implantation depth profiles are obtained by SRIM calculations [42], in quick Kinchin-Pease damage mode using a displacement threshold energy of 40 eV [43].

The damage and injected profiles of both systems are plotted in Figure S1 of Supplementary Material. The subsequent analysis of the samples was performed respectively at 400–500 nm depth in Fe-Ni and at 200–500 nm depth in Ni-Ti. Note that Ni ions of relatively high energy (5 MeV) were used for the irradiation in Ni-Ti to achieve a large damage depth as surface effects is reported to be significant in Ni [44]. From the damage and implantation profiles, the depths at which specimens are lifted out are chosen as far as possible from the surface, while ensuring that the concentration of injected interstitial is negligible. Thereby, the collected data as well as their analysis are assumed not to be biased by PD elimination towards the surface and injected self-interstitial effects as recommended in Ref. [45]. The average point-defect production rate in the investigated range is approximately $\phi = 7.5 \times 10^{-5}$ dpa/s in Ni-Ti and 8.2×10^{-4} dpa/s in Fe-Ni.

2.3. TEM analysis of the microstructure

After irradiation, TEM cross-sectional samples are lifted out using Focused Ion Beam (FIB) equipped on an FEI Helio 650 NanoLab dual-beam Scanning Electron Microscopy (SEM). The lifted out Ni-Ti samples are then electro-polished using flash polishing technique to remove FIB-induced defects [46]. The lifted-out Fe-Ni cross-sectional lamellae are thinned by decreasing the Ga ion voltage from 30 kV to 1 kV up to electron transparency. This procedure leads to high-quality thin foils, without any FIB-induced damage as black dots. The investigation of irradiated microstructure is performed using a 200 kV FEI TECNAI G2 Transmission Electron Microscopy (TEM) equipped with a LaB_6 filament. Bright-Field (BF) mode is employed for defect imaging. Kinematical two-beam conditions are used to optimize dislocation loop contrast. Underfocused condition is used to optimize void contrast. All TEM micrographs are taken for $s_g \geq 0$. The number density of loops is calculated as the counted number of loops divided by the volume of studied zone. The volume is estimated by multiplying the projected area with the sample thickness estimated by the Convergent Electron Beam Diffraction (CBED) technique [47] along the [220] reflection for the Ni-Ti alloy and by STEM/EELS using the log-ratio model for the Fe-Ni alloy.

2.4. APT analysis of the composition distribution

Atom Probe Tomography (APT) needle-shaped specimens are lifted-out and sharpened by FIB. APT analysis is performed using a CAMECA LEAP 4000 HR equipment at a set-point temperature of 50 K in laser-pulsing energy mode at a wavelength of 382 nm, 125 kHz or 200 kHz pulse repetition rate. For each tip, the laser pulse energy was set to an equivalent evaporation fraction of 20% for Fe-Ni and 25% for Ni-Ti. For 3D atom reconstruction, visualization, and data post-treatment, the IVAS software by CAMECA was employed. Both un-irradiated and irradiated samples are analyzed for comparison. Whereas

a homogeneous distribution of Ti and Ni was revealed in unirradiated Ni-Ti and Fe-Ni samples respectively, solute-rich clusters were detected in Fe-Ni irradiated samples and local depletions of titanium were revealed in Ni-Ti irradiated samples. Atomic fraction profiles were obtained using the IVAS algorithm 1D concentration profile. 5 nm diameter cylinders with a fixed bin of 0.5 nm were used for Fe-Ni and 30 nm diameter cylinders with a fixed bin of 1 nm were used for Ni-Ti.

3. Diffusion models and simulation methods

3.1. Atomic fluxes of point defects and solute atoms

Following the Onsager's formalism [48, 49], we express the flux $\boldsymbol{J}_\alpha$ of species α as a linear combination of chemical potential gradients (e.g., $\boldsymbol{\nabla}\mu_\beta$ for species β). We assume that fluxes arising from the vacancy (V) diffusion mechanism and from the self-interstitial atom (in the text abbreviated to SIA, and in the equations to I) diffusion mechanism are additive. In a binary alloy $A(B)$, the flux of atomic species α ($\alpha = A$ or B), reads

$$\boldsymbol{J}_\alpha = \boldsymbol{J}_\alpha^{\mathrm{V}} + \boldsymbol{J}_\alpha^{\mathrm{I}}, \tag{1}$$

with

$$\boldsymbol{J}_\alpha^{\mathrm{V}} = -\frac{1}{k_{\mathrm{B}}T} \sum_{\beta=A,B,\mathrm{V}} L_{\alpha\beta}^{\mathrm{V}} \boldsymbol{\nabla}\mu_\beta, \tag{2}$$

$$\boldsymbol{J}_\alpha^{\mathrm{I}} = -\frac{1}{k_{\mathrm{B}}T} \sum_{\beta=A,B,\mathrm{I}} L_{\alpha\beta}^{\mathrm{I}} \boldsymbol{\nabla}\mu_\beta. \tag{3}$$

Similarly, the fluxes of vacancies and SIAs read

$$\boldsymbol{J}_{\mathrm{V}} = -\frac{1}{k_{\mathrm{B}}T} \sum_{\beta=A,B,\mathrm{V}} L_{\mathrm{V}\beta}^{\mathrm{V}} \boldsymbol{\nabla}\mu_\beta, \tag{4}$$

$$\boldsymbol{J}_{\mathrm{I}} = -\frac{1}{k_{\mathrm{B}}T} \sum_{\beta=A,B,\mathrm{I}} L_{\mathrm{I}\beta}^{\mathrm{I}} \boldsymbol{\nabla}\mu_\beta. \tag{5}$$

In Eqs. (2), (3), (4), and (5), the coefficients $L_{\alpha\beta}^{\mathrm{V}}$ and $L_{\alpha\beta}^{\mathrm{I}}$ are the phenomenological transport coefficients that characterize the diffusion mediated by respectively vacancies and SIAs. For the sake of simplicity, $L_{\alpha\mathrm{V}}^{\mathrm{V}}$ and $L_{\alpha\mathrm{I}}^{\mathrm{I}}$ are respectively denoted $L_{\alpha\mathrm{V}}$ and $L_{\alpha\mathrm{I}}$.

3.2. Thermodynamics of diffusion including elasticity

In this section, we express the PD and alloy thermodynamic driving forces under an applied strain $\underline{\epsilon}$. The isothermal driving forces of diffusion under an applied stress-strain field are the gradients of PD ($d = \mathrm{V, I}$) and alloy chemical potentials [see Eq. (6)]. These chemical potentials locally depend on the stess-strain field.

$$\mu_d = k_{\mathrm{B}}T \ln\left(\frac{C_d}{C_d^{\mathrm{eq}}}\right), \tag{6}$$

where C_d is the atomic fraction of d in the system, and C_d^{eq} is the local equilibrium concentration of d. The latter varies with the local strain and atomic fraction of the solute atoms. The PD equilibrium concentration writes

$$C_d^{\mathrm{eq}} = C_d^{\mathrm{eq,sf}} \exp\left(-\frac{E_d^{\mathrm{el}}}{k_{\mathrm{B}}T}\right), \tag{7}$$

where

$$C_d^{\mathrm{eq,sf}} = C_d^{\mathrm{eq,0}} \left[1 + \frac{C_B(Z_{Bd}^{\mathrm{el}} - Z_{Bd}^0)}{Z_d}\right] \tag{8}$$

is the PD equilibrium concentration in strain-free (sf) system $A(B)$ obtained from a low-temperature expansion formalism [50, 51, 32] for $C_B \gg C_d$. In the above equations, $C_d^{\mathrm{eq,0}}$ is the PD equilibrium concentration in unstrained pure system A, Z_d is the monomer partition function, Z_{Bd}^{el} is the solute-PD pair partition functions including the elastic interactions, Z_{Bd}^0 is the number of solute-PD pair configurations, and E_d^{el} is the elastic contribution to the formation energy of PD under strain $\underline{\epsilon}$. We write E_d^{el} as a sum of two energy terms, where summation over repeated indices is implicit (Einstein convention):

$$E_d^{\mathrm{el}} = -\left[\underline{P}_{ij}^d \epsilon_{ij} + s_d K \operatorname{Tr}(\epsilon)\Omega\right], \tag{9}$$

where $\underline{P}^d$ is the elastic dipole tensor of PD ($d = \mathrm{V, I}$), $\underline{\epsilon}$ is the strain field, K is the bulk modulus, and s_d is the number of created lattice site,

$$s_d = \begin{cases} +1, \text{ for } d = \mathrm{V}, \\ -1, \text{ for } d = \mathrm{I}. \end{cases} \tag{10}$$

The first term in the right-hand side of Eq. (9), $-\underline{P}_{ij}^d \epsilon_{ij}$, describes the energy change due to the relaxation of the system in presence of PD [52]. In presence of PD sources and sinks, PDs are non-conservative species. Their creation or removal entails a variation of the number of lattice sites. For instance, an atom displaced from its original bulk lattice site to the surface or the core of a dislocation creates both a vacancy at the original lattice site and an extra lattice site at the structural defect. The second term, $s_d K \operatorname{Tr}(\underline{\epsilon})\Omega$, corresponds to the work of creating or removing a lattice site under the dislocation-induced strain [53, 54]. We assume the mechanical equilibrium is achieved everywhere, and strain is small enough to remain in the elastic regime.

We assume that, locally, the strain/stress field is uniform. Hence, we may write E_α^{el} as a function of the local stress-strain field. Therefore, a gradient of the elastic strain yields a gradient of E_d^{el}, that modifies the PD driving force. From Eq. (6) and Eq. (8), we write the chemical potential gradient (CPG) of PDs as:

$$\frac{\boldsymbol{\nabla}\mu_d}{k_{\mathrm{B}}T} = \frac{\boldsymbol{\nabla}C_d}{C_d} - \frac{(Z_{Bd} - Z_{Bd}^0)\boldsymbol{\nabla}C_B}{Z_d - C_B(Z_{Bd} - Z_{Bd}^0)}$$
$$- \frac{C_B \boldsymbol{\nabla}Z_{Bd}}{Z_d - C_B(Z_{Bd} - Z_{Bd}^0)} + \frac{\boldsymbol{\nabla}E_d^{\mathrm{el}}}{k_{\mathrm{B}}T}. \tag{11}$$

4

For an alloy $A(B)$, we may write the alloy chemical potential, $\mu_{BA} = \mu_B - \mu_A$, in function of the atomic fraction of monomer B (isolated solute atoms surrounded by A atoms), C_B^{mono} [55],

$$\mu_{BA} = k_{\text{B}}T \ln C_B^{\text{mono}} + H_{\text{s},B}, \tag{12}$$

where $H_{\text{s},B}$ is the solution enthalpy of atom B in A:

$$H_{\text{s},B} = H[N\,A + 1\,B] - H[(N+1)\,A], \tag{13}$$

where $H[N\,A+1\,B]$ is the enthalpy of a system including N atoms A and one atom B. Note that, C_B^{mono} may depend on the solute and vacancy atomic fractions. $H_{\text{s},B}$ depends on strain only. It is written as

$$H_{\text{s},B} = H_{\text{s},B}^0 + E_B^{\text{el}}, \tag{14}$$

where E_B^{el} is the elastic contribution to the solution enthalpy of solute B

$$E_B^{\text{el}} = -\underline{P}_{ij}^B \epsilon_{ij}, \tag{15}$$

Following Eq. (12), we write the CPG of solute atoms as:

$$\frac{\boldsymbol{\nabla}\mu_{BA}}{k_{\text{B}}T} = \frac{1}{C_B^{\text{mono}}}\frac{\partial C_B^{\text{mono}}}{\partial C_B}\boldsymbol{\nabla}C_B$$
$$+ \frac{1}{C_B^{\text{mono}}}\frac{\partial C_B^{\text{mono}}}{\partial C_{\text{V}}}\boldsymbol{\nabla}C_{\text{V}} + \frac{\boldsymbol{\nabla}E_B^{\text{el}}}{k_{\text{B}}T}. \tag{16}$$

We consider the solid solution as a dilute solution in atoms B because, even under high radiation flux, the stationary PD atomic fraction is several orders of magnitudes smaller than the solute one. Accordingly, we may assume that $C_B \gg C_d$ and $C_B^{\text{mono}} = C_B$. Therefore, Eq. (16) simplifies to

$$\frac{\boldsymbol{\nabla}\mu_{BA}}{k_{\text{B}}T} = \frac{\boldsymbol{\nabla}C_B}{C_B} + \frac{\boldsymbol{\nabla}E_B^{\text{el}}}{k_{\text{B}}T}. \tag{17}$$

To conclude, a stress-strain field generates the extra term $\boldsymbol{\nabla}E_\alpha^{\text{el}}$ in the CPGs of PDs and solute atoms. The data of the elastic dipoles ($\underline{P}_{ij}^\alpha$) to compute E_α^{el} are presented in the following section.

3.3. Elastic dipoles of solute atoms and point defects

In Fe-Ni and Ni-Ti alloys, in addition to the elastic dipole of the vacancy and SIA monomers, we include the elastic dipoles of the solute-PD pairs. These dipole tensors are obtained from *ab initio* calculations, following the same numerical scheme presented in Ref. [25].

We have the elastic dipole tensors of the solute-PD pair configurations up to a solute-PD distance equal to a cutting radius (that is far below the kinetic radius). For the solute-SIA pair, the *ab initio* radius is limited to the 5-th nearest neighbour (5-NN) distance in Fe-Ni, and to the 3-NN one in Ni-Ti. Whereas, for the solute-vacancy pair, it is limited to the 10-NN one in Fe-Ni, and the 4-NN one in Ni-Ti. In order to account for the long range PD-solute interactions, we introduce an extrapolation scheme starting

from the pair interactions calculated by DFT. The elastic dipoles of PD ($d = $ V, I) at the k-NN-distance stable configuration are denoted by $\underline{P}_{Bd}^k$. At very large distance, PD and solute do not interact with each other, and the elastic dipole of the solute-PD pair is the sum of the mono-solute ($\underline{P}_B^{\text{mono}}$) and the mono-PD ($\underline{P}_d^{\text{mono}}$) dipoles. Since the elastic interaction of a PD and a solute atom decreases in $1/R^3$ (with R the solute-PD distance) [52], for the sake of simplicity, we assume that the elastic dipoles of the PD-solute pairs seating on k-NN sites (in Fe-Ni, $k > 10$ for vacancy and $k > 5$ for SIAs; and in Ni-Ti, $k > 4$ for vacancy and $k > 3$ for SIAs) are given by

$$\underline{P}_{Bd}^k = \underline{P}_B^{\text{mono}} + \underline{P}_d^{\text{mono}} + (\underline{P}_{Bd}^c - \underline{P}_B^{\text{mono}} - \underline{P}_d^{\text{mono}})\left(\frac{R_c}{R_k}\right)^3, \tag{18}$$

where R_i is the i-NN distance. We set, in Fe-Ni, $c = 10$ for vacancies and $c = 5$ for SIAs; and in Ni-Ti, $c = 4$ for vacancies and $c = 3$ for SIAs.

The elastic dipoles tensors of the solute atoms in different alloys are listed in Table 1. The elastic dipole tensors of the solute-PD pairs in Fe-Ni and Ni-Ti alloys are listed in the Supplementary Material.

3.4. Transport coefficients

Apart from the diffusion driving force, the migration barriers are also modified by the elastic interactions between a chemical species (e.g., PDs or solute atoms) and extended defects, which is the so-called elastodiffusion. The strain effect on the diffusion driving force is conventionally considered to be the major contribution to the absorption bias of SIAs by the PD sinks [7, 38]. In the present study, we neglect the strain effect on the migration barriers of PDs and solute atoms. This assumption greatly simplifies the diffusion equations presented in the following section [Eq. (19)] because the transport coefficients become strain-independent. We will provide in Section 8.3 the possible influence of this assumption on the simulation results. Note that the forced atomic relocation (also called ballistic mixing when relocation events are fully random) in displacement cascades created under ion irradiation changes the PD and solute transport coefficients [56], as well as the RIS behavior [32]. However, this effect is negligible under the present investigated irradiation conditions (see Figure S2 in Supplementary Material). The energy database of the migration barriers in the strain-free system is available in Refs. [28] and [31] for Fe-Ni and in Ref. [25] for Ni-Ti. From the migration barriers, we compute the transport coefficients using the KineCluE code [27].

4. Simulation methods

4.1. Solute redistribution as a solution of the diffusion equation

In the present article, we focus on the edge dislocation loop. Whether the segregated atoms near the loop form

Table 1: Elastic dipole tensors (in eV) of the monomer vacancy, dumbbell, and solute atoms in Fe-Ni and Ni-Ti model alloys.

	Mono-vacancy	Mono-dumbbell ([110] for Fe and [100] for Ni)	Solute atom
Fe-Ni	$\begin{bmatrix} -2.839 & 0 & 0 \\ 0 & -2.839 & 0 \\ 0 & 0 & -2.839 \end{bmatrix}$	$\begin{bmatrix} 23.752 & 4.728 & 0 \\ 4.728 & 23.752 & 0 \\ 0 & 0 & 27.906 \end{bmatrix}$	$\begin{bmatrix} 3.731 & 0 & 0 \\ 0 & 3.731 & 0 \\ 0 & 0 & 3.731 \end{bmatrix}$
Ni-Ti	$\begin{bmatrix} -5.448 & 0 & 0 \\ 0 & -5.448 & 0 \\ 0 & 0 & -5.448 \end{bmatrix}$	$\begin{bmatrix} 25 & 0 & 0 \\ 0 & 24.792 & 0 \\ 0 & 0 & 24.792 \end{bmatrix}$	$\begin{bmatrix} 3.922 & 0 & 0 \\ 0 & 3.922 & 0 \\ 0 & 0 & 3.922 \end{bmatrix}$

a torus or disc-like plate is still an open question. Using APT, Belkacemi et al. [16] observed toroidal clusters of Ni atoms in the Fe-Ni model alloy, corresponding to Ni-decorated dislocation loops. Relying on molecular static simulations, Lu et al. [57] predicted a "disc"-like segregation around faulted dislocation loops in Ni-based concentrated alloys. In the simulation, we assume that the RIS region of the dislocation loop in Fe-Ni is of toroidal form only. However, in Ni-Ti, two different models are investigated by assuming the RIS regions to be toroidal and disc-like. We will compare the different RIS behaviors obtained in Ni-Ti with these two models.

The dislocation loop is considered as a torus/disc centered in a spherical volume. Since the geometries of the torus/disc and the spherical volume are invariant by rotation around the z-axis, a cylindrical coordinate is used. Moreover, we reduce the 3D calculation to a 2D calculation, by solving the diffusion problem in the cross section plane of the dislocation loop (i.e., the z-r plane for a given value of θ in the cylindrical coordinate, cf. Fig. 1-(a) and (b) for a toroidal segregation region and (c) for a disc-like segregation region). We rely on an isotropic approximation of the elastic field to compute the strain/stress field generated by an edge dislocation loop [58]. Previous studies suggest that the dislocation capture radius, r_c, is of order of the Burgers vector (b_v) [59, 60, 61, 62, 63, 38]. In the present study, the capture radius of the dislocation loop is set to $2\,b_v$, which is a typical choice in the literature [38].

Diffusion of the PD ($d =$ V, I) and the solute atom (B) in the vicinity of the dislocation loop within the spherical volume is described by the following system of equations

$$\begin{cases} \frac{\partial C_d}{\partial t} = -\boldsymbol{\nabla} \cdot \boldsymbol{J_d} \\ \frac{\partial C_B}{\partial t} = -\boldsymbol{\nabla} \cdot \boldsymbol{J_B} \end{cases}. \qquad (19)$$

This system of equations is solved in steady-state conditions (i.e., the time derivative of species α is set to zero, $\partial C_\alpha / \partial t = 0$) by means of a finite-difference numerical scheme.

We assume that PDs diffuse and react fast enough with the dislocation such that concentrations of PDs at $r = r_c$, are the equilibrium ones. Therefore, the PD concentration at the inner boundary (Σ_{in}) writes

$$C_d(z, r \in \Sigma_{\text{in}}) = C_d^{\text{eq}}(z, r \in \Sigma_{\text{in}}). \qquad (20)$$

In alloys, C_d^{eq} does not only depend on strain, but also on the local solute concentration [see Eq. (8)]. Hence, it must be computed adaptively in the simulation. Irradiation generates a supersaturation of PDs. We assume that, away from sinks, the PD concentration is uniform and steady on the time scale of PD diffusion across the diffusion area of the investigated dislocation loop. We set the PD concentration at the outer boundary (Σ_{out}) to its steady state bulk value

$$C_d(z, r \in \Sigma_{\text{out}}) = C_d^{\text{out}}, \qquad (21)$$

Note that, depending on the irradiation conditions, the bulk concentration of PDs, C_d^{out}, can be several orders of magnitude larger than the local equilibrium PD concentration. In our simulation, we estimate the supersaturated bulk concentration after a mean-field rate theory [64] including the point-defect creation and recombination phenomena. In order to obtain an estimation of the sink efficiency of the structural defects to absorb PDs, we calculate the sink strength of every class of defects. For the dislocation loop and void classes, there are sink strength models accounting for the average size and density of the defect population. Here, we rely on Jourdan's analytical expression for dislocation loops [38], on Nichols' expressions for voids [65], and on Raul's expression for dislocation lines [64].

In both Fe-Ni and Ni-Ti alloys, we do not account for a possible absorption or removal of solute atoms at the dislocation, which is equivalent to ignoring an effect of the dislocation climbing on solute RIS. Therefore, the normal flux of solute atoms at the inner boundary is set to zero:

$$\boldsymbol{n} \cdot \boldsymbol{J_B}(z, r \in \Sigma_{\text{in}}) = 0, \qquad (22)$$

where $\boldsymbol{n}$ is the unit vector normal to the inner boundary. We set the solute concentration at the outer boundary (i.e., the bulk value) to C_B^{out} which is changed adaptively in the simulation such that the average solute concentration equals the effective nominal solute atom concentration, C_B^{n}, extracted from the APT analysis

$$C_B(z, r \in \Sigma_{\text{out}}) = C_B^{\text{out}}. \qquad (23)$$

The fluxes of PDs and solute atoms crossing the sym-
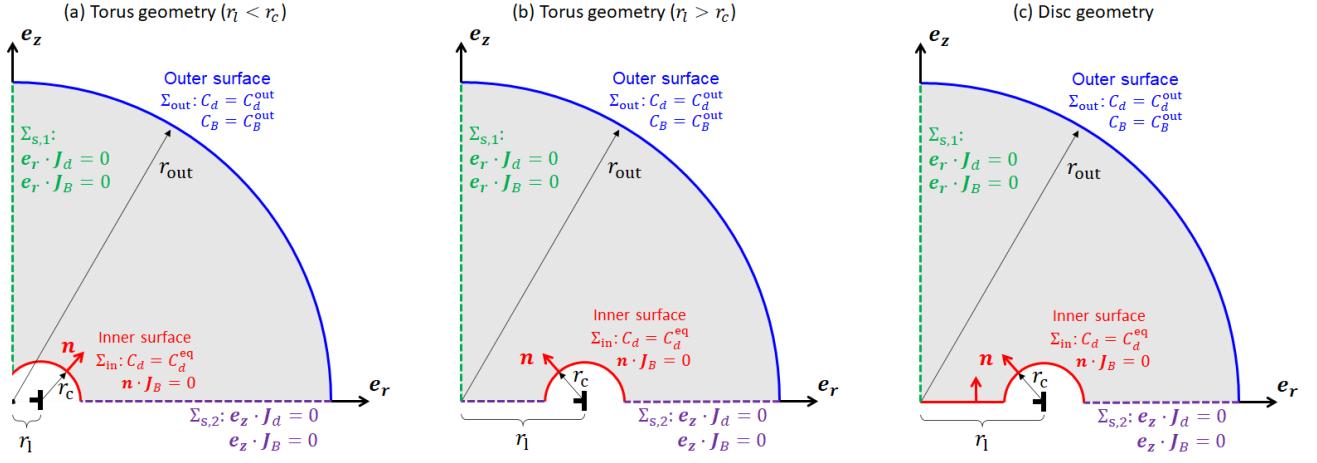
Figure 1: Geometries used to solve the PD and solute diffusion equations around a dislocation loop with (a) torus form and $r_l < r_c$, (b) torus form and $r_l > r_c$, (c) disc form. At the blue outer boundary (Σ_{out}), the PD and solute concentrations is set to be the bulk concentration C_d^{out} and C_B^{out}, respectively. At the red inner boundary (Σ_{in}) the PD concentration is imposed to be the equilibrium one C_d^{eq}, whereas the solute flux across Σ_{in} is set to zero. The point-defect and solute fluxes across the green and purple boundaries ($\Sigma_{\text{s},1}$ and $\Sigma_{\text{s},2}$) are fixed to zero.

metric boundaries $\Sigma_{\text{s},1}$ and $\Sigma_{\text{s},2}$ are set to zero:

$$e_r \cdot J_{B \text{ or } d}(z, r \in \Sigma_{\text{s},1}) = 0 \qquad (24)$$

$$e_z \cdot J_{B \text{ or } d}(z, r \in \Sigma_{\text{s},2}) = 0, \qquad (25)$$

where e_r and e_z are the unit vectors of the orthogonal basis in the z-r plane.

4.2. Modeling of the microstructure dispersion

The spatial distribution of dislocation loops can be very heterogeneous (see an example of microstructure measured after irradiation as presented in Section 5). The variation of the local dislocation loop density may locally affect the RIS. Hence, RIS at dislocation loops can be very different from one to another even though their radius are similar. It has been shown that the local density of dislocation loops is not related to their radius [39]. In order to tackle these local effects, we circumscribe every dislocation loop by its Voronoi volume. It is defined in such a way that it contains all the points in space that are closer to the center of the loop than to those of the other loops. In order to keep the symmetry of the dislocation loop, we assume the Voronoi volume to be a sphere. In this case, the loop is systematically in the center of the sphere, as presented in Fig. 1. In the limiting case of a homogeneous distribution of dislocation loops, every loop has the same average Voronoi volume ($\overline{V_v}$) that is related to the average loop density ($\overline{\rho}$): $\overline{V_v} = 1/\overline{\rho}$. In all other situations where the elastic interactions between the loops may be ignored, the dislocation loops are randomly distributed in space. According to Refs. [66, 39], the probability distribution of the Voronoi volumes of dislocation loops, (V_v), normalized by the average volume, ($\overline{V_v}$), follows the Poisson-Voronoi distribution (i.e., a special case of the gamma distribution).

The analytical expression of this distribution reads [67]

$$p_v(v) = \frac{v^{\gamma-1}}{\beta^\gamma \Gamma(\gamma)} \exp\left(-\frac{v}{\beta}\right), \qquad (26)$$

with

$$v = \frac{V_v}{\overline{V_v}}. \qquad (27)$$

Γ is the gamma function, and β and γ are two parameters. Lazar et al. [68] have investigated the numerous points randomly distributed in space and their Voronoi volumes. Based on a simulation data set of a combined total of $250\,000\,000$ volumes, they show that all of them follow a Poisson-Voronoi probability distribution. From the data set, they have determined the β and γ parameters: $\beta = 0.1790$ and $\gamma = 1/\beta = 5.586$. The mean value and the standard deviation of this distribution are respectively $\overline{v} = 1$ and $\sigma = \sqrt{\beta} = 0.42$.

As reported in Ref. [39], there is no direct relationship between the radius and the Voronoi volume of the dislocation loop. Therefore, by assuming that these two variables are independent, we can express the joint probability distribution of the Voronoi volume/dislocation loop radius pair, $p_{v,r}$, as a product of the two individual distributions [Eqs. (26) and (29)]

$$p_{v,r}(v, r_l) = p_v(v)\, p_r(r_l). \qquad (28)$$

4.3. Statistical approach of solute concentrations obtained from APT

To mimic the experimental measurement of a local solute concentration by APT, we introduce a cylindrical control volume identical to the one used in APT. Note that the radius of the cylinder differs between Fe-Ni and Ni-Ti: it is equal to $3.5\,\text{nm}$ for Fe-Ni and $30\,\text{nm}$ for Ni-Ti. For the simulation of APT 1D-concentration profiles, we

assume that the geometric center of the control volume coincide with the center of the dislocation loop. Note that the radius of the control volume is larger than those of the investigated dislocation loops. Hence, in the simulation, the control volume entirely contains the dislocation loop. As in the experimental protocol, the control volume is equally divided into slices along the longitudinal direction. The width of each slice is set to 0.5 nm for Fe-Ni and 1.0 nm for Ni-Ti, which are the values of the present APT analysis. We then calculate the average solute concentration in each slice. It forms the 1D concentration profile along the longitudinal direction of the cylinder. Obviously, the resulting concentration profile depends on the direction of the cylinder with respect to the habit plane of the dislocation loop. In most APT analysis, we do not have access to the direction of the habit plane, because the crystallographic orientation of the specimen is undetermined, or the specimen does not entirely contains the dislocation loop, or it is hard to precisely localize the dislocation loop. In the present modeling study, we consider two limiting cases: (1) the first one is when the longitudinal direction of the cylinder (denoted by $\boldsymbol{u}_{\mathrm{APT}}$) is perpendicular to the Burgers vector of the dislocation loop ($\boldsymbol{b}_{\mathrm{v}}$); and (2) the second one corresponds to the case where $\boldsymbol{u}_{\mathrm{APT}}$ is parallel to $\boldsymbol{b}_{\mathrm{v}}$. Note that since the simulated dislocation loop is an edge dislocation, the corresponding Burgers vector is perpendicular to its habit plane.

In low density dislocation systems such as the Ni-Ti system, the volume of the APT specimen may be significantly smaller than the average Voronoi volume. This is a case where the solute concentration of the APT volume may be very different from the effective nominal concentration of the sample. In order to reproduce the dispersion of the solute concentration extracted from a set of APT specimens, we combine the solute concentration field post-treatment with a statistical simulation method as follows:

1. We sample a (Voronoi volume, dislocation loop radius) pair combination, (v, r_{l}), after their joint probability distribution.
2. Within the sampled Voronoi volume, we randomly choose a center of the cylindrical APT volume. The longitudinal direction of the control volume is also randomly chosen.
3. We then calculate the average solute concentration of the APT control volume. Note that if the control volume center is close to the outer boundary of the Voronoi volume, we set the concentration of the volume that leaves the Voronoi area to the corresponding bulk value, $C_{\mathrm{Ti}}^{\mathrm{out}}$.
4. Steps 1–3 are repeated until the obtained density histogram of the solute concentration is nearly converged ($> 10^4$ times).

5. Microstructural analysis

The microstructural characterization by TEM of the Fe-Ni sample revealed the absence of voids and the presence of a high density of small dislocation loops (cf. Fig. 2). Radiation-induced nanometric dislocation loops were so small and numerous that their individual tracing was impossible when tilting the sample so as to reach a desired diffraction condition. Therefore, the statistical method developed by A. Prokhodtseva et al. [69], based on the invisibility criterion [70], was applied to estimate their total number density, which is equal to $2.0 \times 10^{22}\,\mathrm{m}^{-3}$. The histogram of the loop radius for a total of 3231 loops is shown in Fig. 3. According to the experimental histogram, the mean radius is equal to 1.5 nm, which is close to the resolution limit of TEM (about 1 nm). In this case, the number of loops with small radius ($< 1\,\mathrm{nm}$) can be largely underestimated, as reported in Ref. [71, 23]. Therefore, in order to extrapolate the loop size distribution at radii below 1 nm, we introduce a fitting function of the loop distribution, the parameters of which are adjusted so that to reproduce the experimental histogram (Fig. 3) at loop radii larger than 1 nm. The chosen fitting function, p_{r}, is the gamma distribution exhibiting a similar shape as the experimental histogram, tending to 0 when the loop radius $r_{\mathrm{l}} \rightarrow +\infty$. The expression of (p_{r}) is the following

$$p_{\mathrm{r}}(r_{\mathrm{l}}) = \frac{r_{\mathrm{l}}^{a-1}}{b^a \Gamma(a)} \exp\left(-\frac{r_{\mathrm{l}}}{b}\right), \qquad (29)$$

where r_{l} is the loop radius (in nm), and a and b are two fitting parameters. We obtain $a = 0.621$ and $b = 0.951$. The obtained regression coefficient R^2 is 0.98, marking a very satisfactory correlation. We extrapolate the loop distribution down to $r_{\mathrm{l}} = 0.125\,\mathrm{nm}$, nearly corresponding to the radius of a single PD. The fitted histogram function predicts a much higher number of loops with radius smaller than 1 nm, with a resulting total loop number of 9034, which is well above the measured one, 3231, obtained from a direct TEM observation. Therefore, according to the fitted histogram, the mean loop radius $\overline{r_{\mathrm{l}}} = ab = 0.6\,\mathrm{nm}$ and the dislocation density is $5.6 \times 10^{22}\,\mathrm{m}^{-3}$.

The spatial distribution of loops is rather homogeneous at the micron scale as presented in Fig. 2-(a). Whereas it is far from being homogeneous at smaller scales, as illustrated in Fig. 2-(c) and (d). Note that the volume of the area shown in Fig. 2-(c) or (d) is close to the average Voronoi volume, that contains in average, a single dislocation loop.

In the Ni-Ti samples, the three extended defects— cavities, dislocation lines, and loops—are the major extended defects observed in the investigated domain. Their average sizes and densities are summarized in Table 2. Among these three types of defects, dislocation loops are the dominant features of the microstructure (cf. Fig. 4). They are interstitial-type $1/3 < 111 >$ Frank loops and $1/2 < 110 >$ perfect loops. According to the experimental histogram for 239 loops (cf. Fig. 5), their radii range from 0.8 to 35.5 nm in the investigated domain and the average one equals 8.5 nm. Moreover, the loop density is $1.3 \times 10^{21}\,\mathrm{m}^{-3}$. Here again, as shown in the case of Fe-Ni,
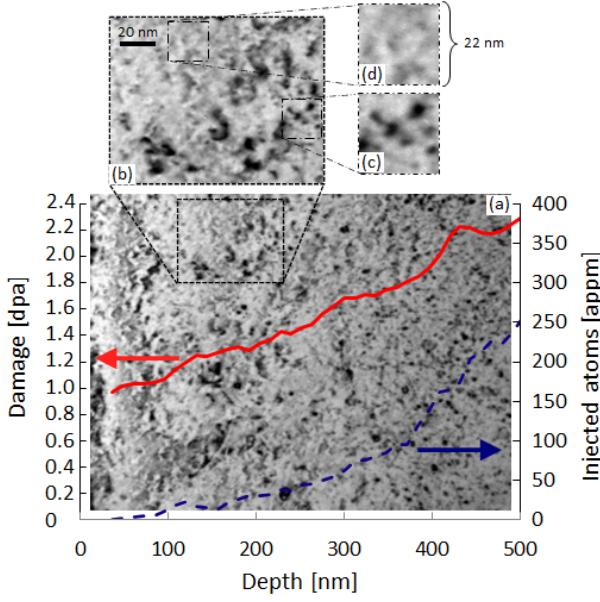
Figure 2: Microstructure of an irradiated Fe-Ni sample characterized by transmission electron microscopy. The solid and dashed lines respectively represent the irradiation damage and injected atom profiles calculated by the Stopping Range of Ions in Matter (SRIM) code [72] using the Kinchin-Pease option with a displacement threshold energy of 40 eV [73].
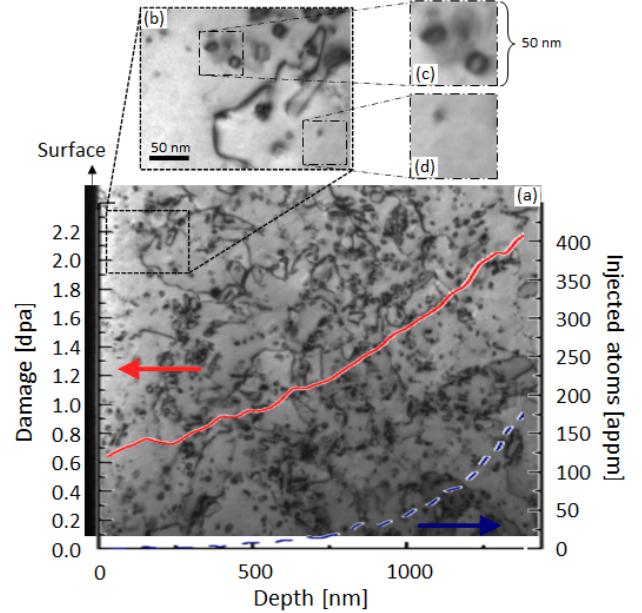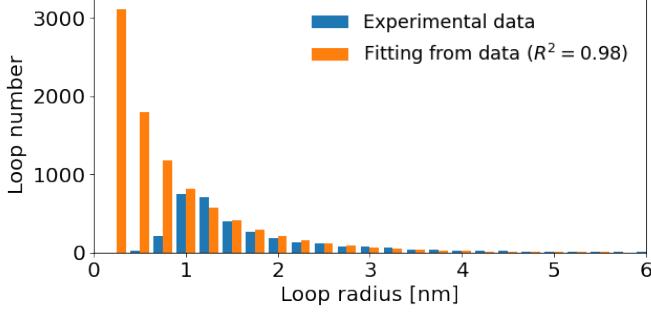

Figure 4: Microstructure of the irradiated Ni-Ti sample characterized by transmission electron microscopy. The solid and dashed lines respectively represent the irradiation damage and injected atom profiles given by SRIM.

Figure 3: Histograms of the dislocation loop radius distribution in the irradiated Fe-Ni sample as measured by TEM, and interpolated by the gamma distribution function.

Figure 5: Histograms of loop radius in irradiated Ni-Ti obtained from experimental measurement and fitting from these data using the gamma distribution function.

we provide a fitting gamma distribution function of the experimental histogram for loops with radii larger than 1 nm. Parameters of Eq. (29) are set to $a = 2.218$ and $b = 3.10$. The regression coefficient is equal to $R^2 = 0.87$. Thereby, the fitted gamma distribution function does not reproduce the experimental histogram as well as in the case of the Fe-Ni system. This can be explained by the lower total loop number measured in Ni-Ti. The fitted histogram predicts a higher number of loops with radius equal to 1 nm. Nevertheless, most of the loops in Ni-Ti have a radius larger than the TEM resolution limit (which is around 1 nm). Therefore, the total loop number predicted by the fitted histogram (238) is almost equal to the value directly obtained from the experimental histogram (239). Finally, according to the fitted histogram, the mean loop radius

is 7.0 nm and the dislocation density is the same as the measured one ($1.3 \times 10^{21} \, \text{m}^{-3}$).

Table 2: Overview of the experimentally observed microstructure in the irradiated Ni-Ti model alloy. The value in parenthesis indicates the average loop radius extracted from the fitted histogram.

Defect	Dislocation loops	Dislocation lines	Cavities
Average density	$1.2 \times 10^{21} \, \text{m}^{-3}$	$3.8 \times 10^{13} \, \text{m}^{-2}$	$2.0 \times 10^{20} \, \text{m}^{-3}$
Average radius	8.5 (7.0) nm	N/A^1	8.0 nm

[1]The radius of the dislocation line is set to its capture radius, because it was not measured.

As observed in Fe-Ni, the density of dislocation loops

is very heterogeneous at the scale of the average Voronoi volume, as for example we find 4 loops in Fig. 4-(c), while only 1 loop in Fig. 4-(d).

6. Experimental characterization of solute redistribution

Our investigation of solute redistribution mainly relies on the APT technique. The dislocation density in Fe-Ni is one order of magnitude higher than in Ni-Ti. Thus, in Fe-Ni, Voronoi volumes are much smaller than the volume of a typical APT specimen, while, in Ni-Ti, Voronoi volumes are larger than the ones of APT specimens. Therefore, we expect that each Fe-Ni APT specimen contains numerous dislocation loops, contrary to Ni-Ti APT specimens where few dislocation loops are captured.

In the Fe-Ni system, prior to irradiation, solute atoms are homogeneously distributed in the Fe-rich matrix, as expected for this undersaturated alloy [74]. As mentioned in Section 2.1, the nominal Ni composition is 3.30 at.%. Upon irradiation, three APT specimens were analyzed. Their average Ni content was measured to be 2.70 at.%. The loss in Ni is certainly due to a redistribution of Ni atoms on a scale larger than that of a APT specimen volume, probably resulting from defects with densities smaller than the one of dislocation loops. Since our aim is to account for the solute redistribution resulting from the formation of dislocation loops, we choose to set the effective nominal concentration, C_{Ni}^{n}, to 2.70 at.%, instead of the nominal concentration (3.30 at.% at.%). Every APT specimen extracted from the irradiated sample contains Ni-rich clusters. One of them is given as an example in Fig. 6. The 3D reconstructed volume reveals the presence of numerous spherical Ni-rich clusters among which, one exhibiting a toroidal shape. Their mean number density is $1.4 \pm 0.2 \times 10^{23}$ m^{-3}. These clusters contain up to 55.0 at.% Ni.

In the Ni-Ti system, APT analysis of five unirradiated samples indicates that Ti is homogeneously distributed before irradiation. Eight APT specimens are lifted from one irradiated sample, at a depth ranging from 200 to 500 nm of the irradiated zone. The APT collected data are summarized in Table 3. The average volume of these specimens is 2.6×10^5 nm^3, which corresponds to approximately one third of the average Voronoi volume of a dislocation loop (7.7×10^5 nm^3). Therefore, we expect that two to three ($8 \times 1/3$) dislocation loops may be captured in the APT specimen set. The average Ti content of the analyzed specimens is approximately 0.48 at.%, which is equal to the nominal concentration of the Ni-Ti macroscopic sample. It is worthy noting that, though the average composition is the nominal one, we observe a dispersion of the Ti content among the various APT specimens. As shown in Table 3, the Ti content ranges from 0.29 to 0.65 at.%. In specimens 1–7, the Ti content distribution is relatively homogeneous: no fluctuation significantly higher than the

uncertainty is identified, implying that no extended defects are captured. In specimen 8, two Ti depleted zones are detected. The 3D reconstructed volumes (presented in the middle of Fig. 7) shows the two Ti-depleted zones. Besides, away from the depleted zones, Ni content is slightly increased. Since both depleted zones are curved, it is very likely that they do not correspond to segregation areas of a dislocation line. Moreover, they are probably not associated with voids because there is no local variation of the atomic density. Therefore, they may correspond either to two separate dislocation loops or to two segments of a large dislocation loop. In the latter case, the loop radius of the large dislocation loop would be at least 35 nm, according to the relative positions of the two Ti-depleted zones. However, after the loop radius histogram obtained by TEM (Fig. 5), it is almost impossible to find such a large loop in the microstructure. Hence, we assume that the two Ti-depleted zones are associated with two individual dislocation loops.

7. Simulation of solute redistribution

Under irradiation, solute redistributes in the vicinity of PD sinks and away from sinks. As explained above, dislocation loops are the major sinks in both systems. Hence, we choose to reduce the microstructure to an ensemble of dislocation loops connected to each other by their volumes of Voronoi. We assume that RIS at the dislocation loop within every Voronoi's volume adds up to yield the overall solute redistribution of the microstructure. The distribution of both the Voronoi's volumes and dislocation loop radii have been deduced from the TEM characterization of the microstructure (cf. Section 5). Following the approach presented in Section 3, we perform simulations of the radiation-induced solute redistribution around a dislocation loop. Representative values of Voronoi volumes and loop radii are sampled according to the Poisson-Voronoi distribution and the fitted histogram function of loop radii, in order to reproduce the dispersion of the local microstructure under irradiation. The chosen values of the normalized Voronoi volumes [Eq. (27)] range from $1 - 2\sigma$ to $1 + 3\sigma$, covering over 99% of the volumes of the distribution. We sample the loop radii after their histograms. We set the loop radius $r_l = n \overline{r_l}$ with $\overline{r_l}$ the average loop radius obtained from the fitted histogram, and $n = 0.5, 1.0, 1.5, 2.0, 2.5, 3.0$. From the solution of the diffusion/reaction equation [Eq. (19)] within a given Voronoi volume, we obtain the 2D redistribution of solute atoms around the dislocation loop. We then perform a post-treatment of the solute concentration field, in order to account for the finite size effects of the APT sampling volumes commonly employed to extract RIS-1D profiles, as illustrated in Fig. 6 and in Fig. 7. The post-treatment method is presented in Section 4.3. Then, we present a statistical analysis of the solute concentration away from sinks depending on the dispersion of loop radius and density.
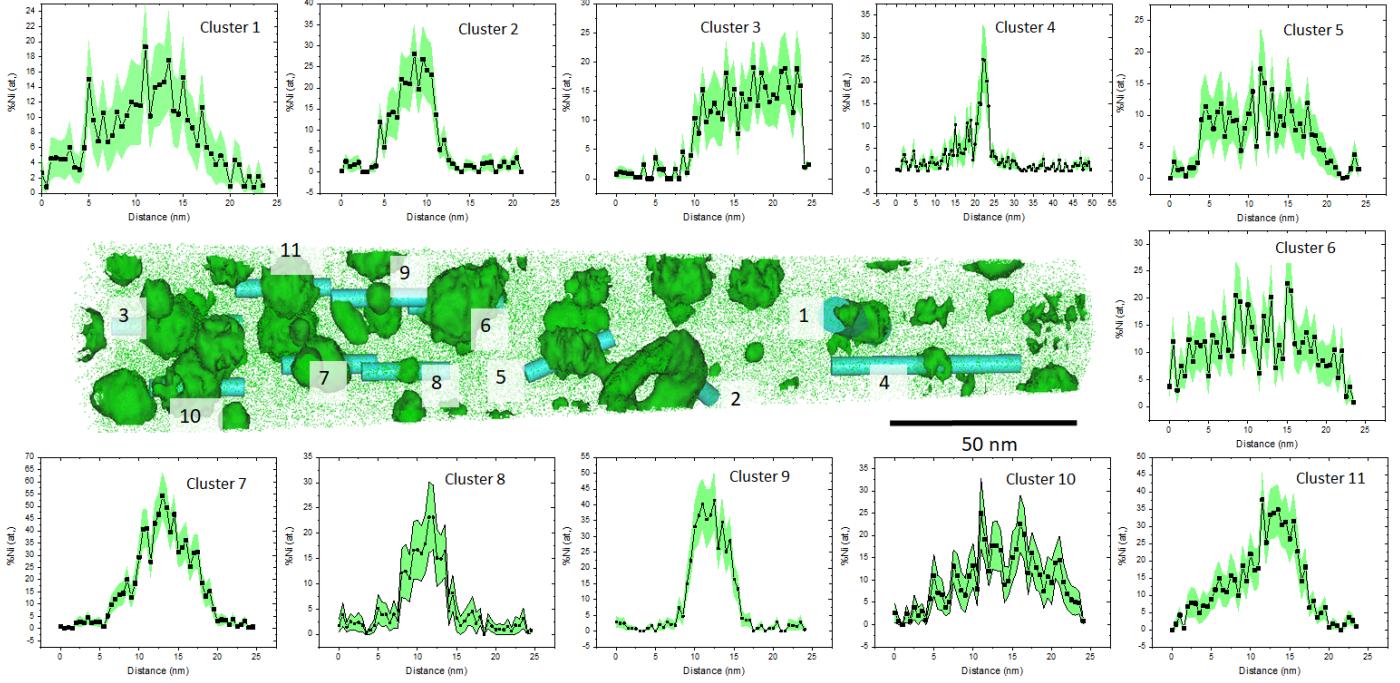
Figure 6: APT analysis of nickel (in green) distribution in Fe-Ni (in the middle) and the uni-dimensional depletion profiles crossing segments of potential dislocation loops. The square symbols of the uni-dimensional profiles represent the measured local Ni composition, and the shaded areas indicate the uncertainty domain.

Table 3: Volumes and Measured compositions in Ti of the eight specimens lifted from the Ni-Ti irradiated alloy.

No.	1	2	3	4	5	6	7	8	Average 1–8
Mean Ti% at.	0.46	0.58	0.58	0.52	0.40	0.29	0.65	0.40	0.48
Standard error	0.004	0.004	0.003	0.002	0.003	0.004	0.009	0.002	0.004
Volume [10^4 nm^3]	16	12	61	34	9	9	12	56	26

7.1. Radiation induced segregation

We present in Fig. 8 the Ni concentration field around a dislocation loop with a radius equal to the average one, and for various Voronoi volumes. We predict a Ni enrichment in the tensile region of the dislocation loop, while a Ni depletion in the compressive region. A signature of the overall Ni enrichment is the slight decrease of the Ni content at the outer boundary of the Voronoi volume ($C_{\mathrm{Ni}}^{\mathrm{out}}$). The Ni concentration field around the dislocation loop does not vary much with the size of the Voronoi volume. The simulation results presented in Fig. 8 show that the highest Ni atomic fraction at the dislocation loop is around 17 at.%, and the Ni atomic fraction away from the dislocation loop (corresponding to the atomic fraction of Ni at the outer boundary) ranges from 2.61 at.% to 2.67 at.%.

In Fig. 9, we plot the Ni concentration field around a dislocation loop, for the average Voronoi volume, at various values of the dislocation loop radius. The Ni radiation induced redistribution is very sensitive to the dislocation loop radius. The highest Ni atomic fraction in the tensile region of the dislocation loop increases with the loop radius: from 10 at.% ($r_l = 0.5\,\overline{r_l}$) to 43 at.% ($r_l = 3\,\overline{r_l}$). As for the atomic fraction of Ni away from the loop, $C_{\mathrm{Ni}}^{\mathrm{out}}$, it

decreases with the loop radius: from 2.68 at.% ($r_l = 0.5\,\overline{r_l}$) to 2.58 at.% ($r_l = 3\,\overline{r_l}$). Note that the smallest dislocation loops ($r_l = 0.5\,\overline{r_l}$) exhibit a radius which is even smaller than the capture radius. In this case, PDs are captured by the dislocation before reaching the compressive region. The resulting RIS of Ni is mainly controlled by the tensile strain.

A reconstruction of the 3D concentration field by applying the symmetry operations (e.g., a 2π-rotation around the z-axis) leads to nearly-spherical solute enrichment of small loops ($r_l \leq \overline{r_l}$), and toroidal-shape Ni enrichment of larger loops ($r_l \geq 2\,\overline{r_l}$). According to the fitted histogram of dislocation loop radius (Fig. 3), most of the dislocation loops are of radius smaller than $\overline{r_l}$. This explains why Ni-enriched regions detected by APT are spherical (cf. Fig. 6).

Note that in the simulation, dislocation loops in Fe-Ni are assumed to be of interstitial-type. The Ni concentration field around a vacancy loop can be obtained by following the same numerical scheme with a strain field opposite to the one generated by an interstitial loop. The relaxation volume of a substitutional Ni atom in Fe being positive, drives Ni towards the tensile region of the dislocation loop. Therefore, Ni atoms are enriched at the outer
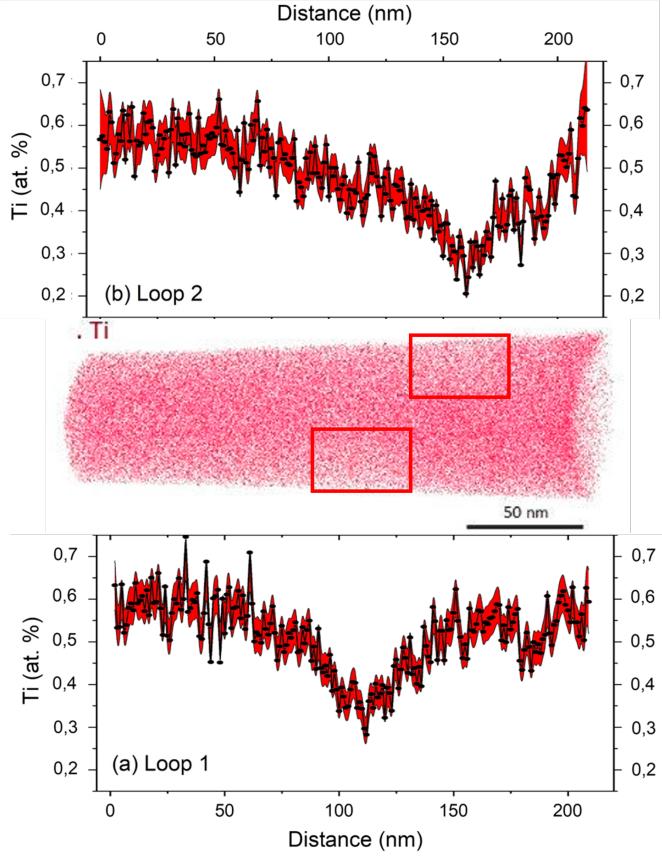
11

Figure 7: APT reconstruction of the irradiated alloy specimen no. 8 in Ni-Ti showing the three-dimensional repartition of 50% of titanium atoms (middle). The APT reconstruction is superimposed with the 2D titanium concentration plot. The red squares highlight the Ti depletion zones where the uni-dimensional depletion profiles crossing (a) loop 1 and (b) loop 2 along the specimen are extracted. The dots in the profiles represent the measured local Ti composition, and the shaded areas indicate the associated statistical error.

region of the interstitial loop, and at the inner region of the vacancy loop. In Figure S3 of the Supplementary Material, we show the calculated Ni solute redistribution in the vicinity of a vacancy dislocation of a relatively large radius $3\,\overline{r_l}$, has a disc-shape symmetry. Since Ni-enriched regions detected by APT of large loops ($r_l \geq 2\,\overline{r_l}$) are of toroidal shape (e.g., Cluster 2 in Fig. 6), dislocation loops in Fe-Ni are likely to be interstitial ones, justifying our assumption.

The Ni content at the outer boundary, $C_{\mathrm{Ni}}^{\mathrm{out}}$, depends both on the Voronoi volume and the loop radius. For a more complete investigation of $C_{\mathrm{Ni}}^{\mathrm{out}}$, we perform RIS calculations for a total of 36 combinations of the (loop radius/Voronoi volume) pair. The results are plotted in Fig. 10. $C_{\mathrm{Ni}}^{\mathrm{out}}$ ranges from 2.45 at.% for a large loop ($r_l = 3\,\overline{r_l}$) in a small Voronoi volume ($v = 1 - 2\,\sigma$), while it is nearly equal to the effective nominal concentration (2.68 at.%) for a small loop ($r_l = 0.5\,\overline{r_l}$) in a big Voronoi volume ($v = 1 + 3\,\sigma$). After Eq. (28), we compute the joint probabilities of the 36 loop radius/Voronoi volume pairs, and provide the corresponding probability distribution of

the Ni atomic fraction away from the dislocation, $C_{\mathrm{Ti}}^{\mathrm{out}}$ (cf. Fig. 15). The probability ($P_{[C_1,\,C_2[}$) of $C_{\mathrm{Ti}}^{\mathrm{out}} \in [C_1,\,C_2[$ is given by

$$P_{[C_1,\,C_2[} = \frac{\sum\limits_{(v,r_l)\in\mathscr{S}_{[C_1,\,C_2[}} p_{\mathrm{v,r}}(v,r_l)}{\sum\limits_{\mathrm{all\ 36\ }(v,r_l)} p_{\mathrm{v,r}}(v,r_l)}, \tag{30}$$

where $\mathscr{S}_{[C_1,\,C_2[}$ is the set of all possible combinations (v, r_l) that give $C_{\mathrm{Ni}}^{\mathrm{out}} \in [C_1,\,C_2[$ among the 36 combinations. According to the distribution shown in Fig. 11, in most cases (over 99% of probability), $C_{\mathrm{Ni}}^{\mathrm{out}}$ is between 2.54 at.% and 2.70 at.%. The probabilities of the combinations $(v, r_l) = (1 - 2\,\sigma,\, 3\,\overline{r_l})$ and $(1 - \sigma,\, 3\,\overline{r_l})$ are so small that it is almost impossible to observe $C_{\mathrm{Ni}}^{\mathrm{out}} < 2.54$ at.%. Therefore, in most cases, the maximum decrease of $C_{\mathrm{Ni}}^{\mathrm{out}}$ resulting from a Ni enrichment at dislocation loops is -0.26 at.% (corresponding to a relative decrease of about 10% of the effective nominal concentration).

In the Ni-Ti system, Fig. 12 shows the Ti concentration field around a dislocation loop for a radius set to its average value and various Voronoi volumes, given by both toroidal and disc-like RIS models. In agreement with the stress-free calculation of flux couplings in Ni-Ti [25], we predict a depletion in Ti around the dislocation loop.

The elastic interactions between the dislocation loop and PDs do not change the sign of RIS, at least at $T = 450\,^\circ\mathrm{C}$. The Ti depleted-region given by disc-like RIS model is slightly larger than that from a toroidal RIS model, whereas the overall Ti concentration fields obtained with these two models are very similar. Note that the Ti depletion is greater in the compressive region than in the tensile region. This depleted zone around the dislocation loop leads to a dramatic increase of the Ti content at the outer boundary of the Voronoi volume. The variation of Voronoi volumes does not significantly change the redistribution of Ti close to the dislocation loop, whereas it affects the Ti concentration away from the dislocation. $C_{\mathrm{Ti}}^{\mathrm{out}}$ significantly decreases with the Voronoi volume for both disc-like and toroidal RIS models: from 0.55 at.% at $V_{\mathrm{v}} = (1 - 2\sigma)\overline{V_{\mathrm{v}}} = 1.2 \times 10^5\,\mathrm{nm}^3$, to 0.50 at.% at $V_{\mathrm{v}} = (1 + \sigma)\overline{V_{\mathrm{v}}} = 1.1 \times 10^6\,\mathrm{nm}^3$.

We plot, in Fig. 13, the Ti redistribution around the dislocation loop at the average Voronoi volume for different values of loop radius, given by both toroidal and disc-like RIS models. For relatively small dislocation loops ($r_l \leq \overline{r_l}$), we obtain very similar Ti concentration fields using the two RIS models. However, for loop radii $r_l > \overline{r_l}$, the Ti depletion region given by a disc-like model is much larger than than from a toroidal model, because Ti is depleted in the entire disc-plate inside the dislocation loop. In both models, a change of the loop radius leads not only to very different Ti concentration profiles near the loop, but also to different Ti atomic fractions at the outer boundary. The latter increase with the loop radius. Using a toroidal RIS model, $C_{\mathrm{Ti}}^{\mathrm{out}}$ increases from 0.50 at.% ($r_l = 0.5\,\overline{r_l} = 3.5\,\mathrm{nm}$) to 0.56 at.% ($r_l = 3\,\overline{r_l} = 21\,\mathrm{nm}$), whereas using a disc-like
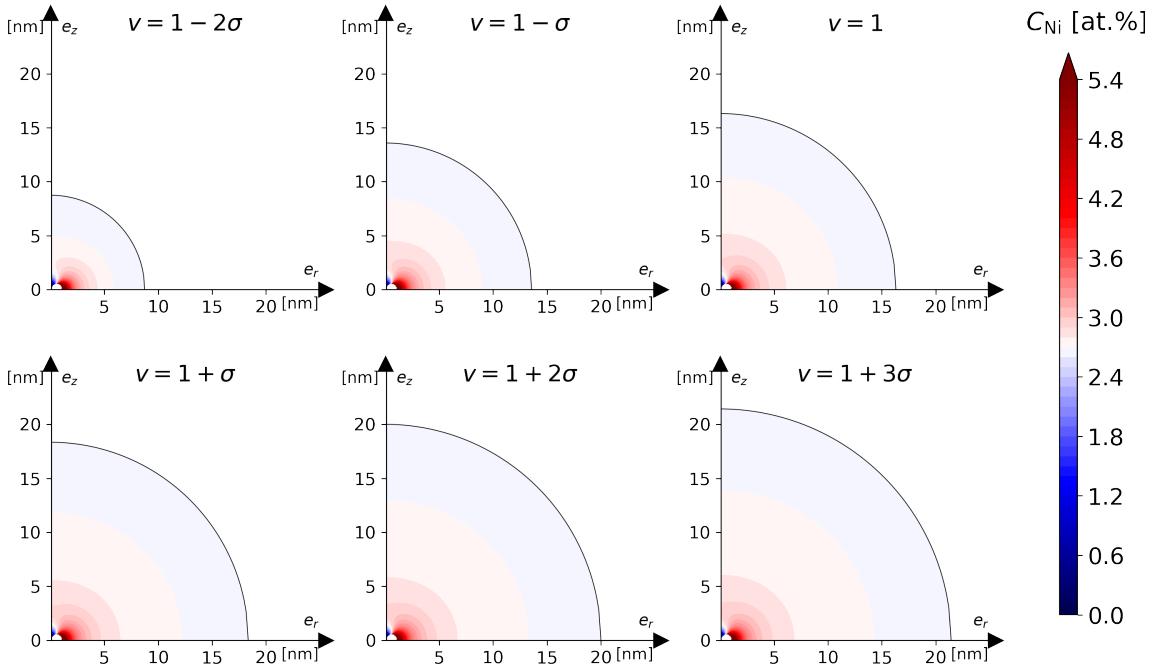
Figure 8: The Ni concentration redistribution around a dislocation loop in Fe-Ni for various Voronoi's volumes. $v = V_v / \overline{V_v}$ is the ratio between the simulated Voronoi's volume (V_v) and the average one ($\overline{V_v}$). $\sigma = 0.42$ is the standard deviation of the Poisson-Voronoi distribution. The average Voronoi volume is set to $1.8 \times 10^4 \, \text{nm}^3$ and the loop radius is set to the average value (0.6 nm). The effective nominal Ni concentration C_{Ni}^n is set to 2.70 at.%., the temperature is 400 °C, and the damage production rate is 9×10^{-4} dpa/s.
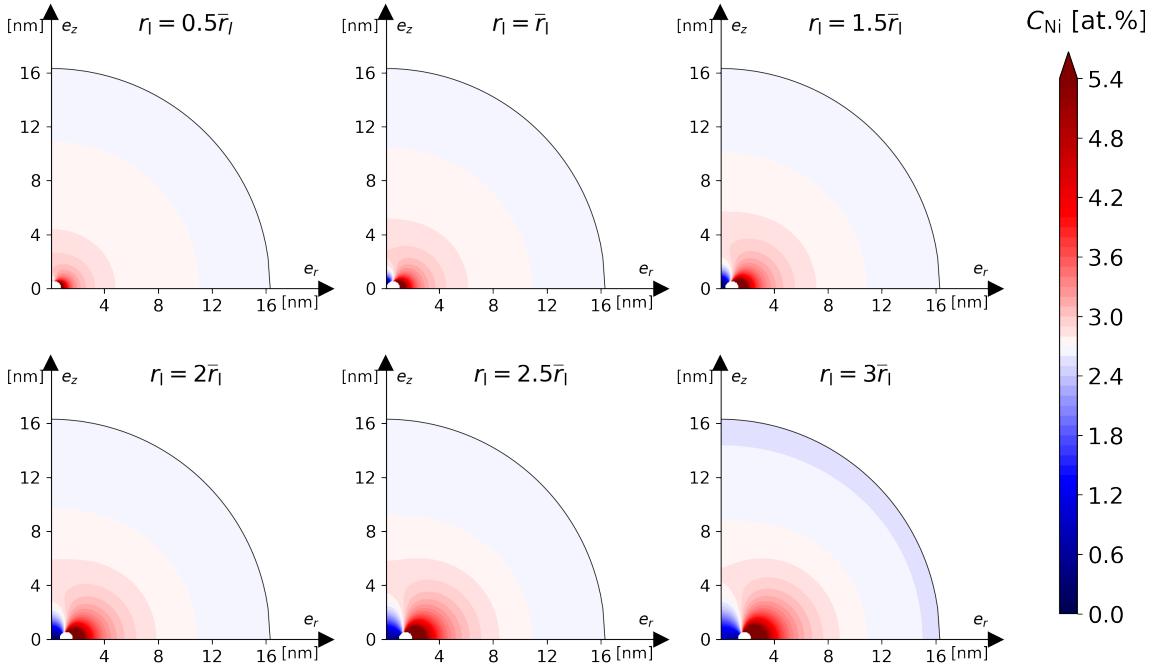
Figure 9: The Ni concentration distribution around a dislocation loop for in Fe-Ni various loop radii. $\overline{r_l} = 0.6 \, \text{nm}$ is the average loop radius. The Voronoi's volume is set to its average value ($1.8 \times 10^4 \, \text{nm}^3$). The effective nominal Ni concentration C_{Ni}^n is set to 2.70 at.%., the temperature is 400 °C, and the damage production rate is 9×10^{-4} dpa/s.

13
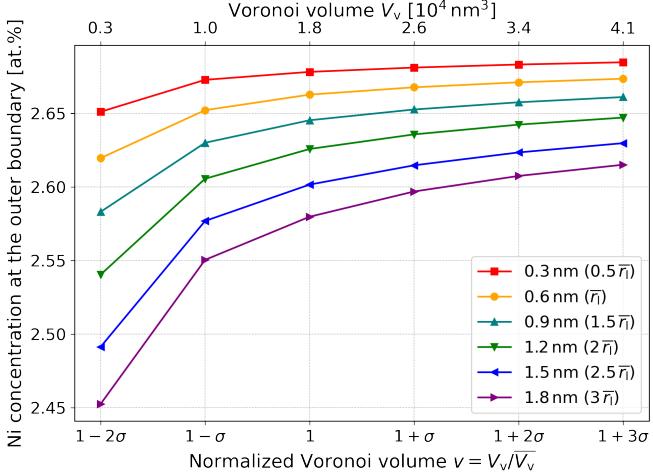
Figure 10: The distribution of the bulk Ni concentration at the outer boundary in Fe-Ni obtained for various Voronoi's volumes and dislocation loop radii. $\overline{r_l} = 0.6$ nm is the average loop radius. The effective nominal Ni concentration C_{Ni}^n is set to 2.70 at.%., the temperature is 400 °C, and the damage production rate is 9×10^{-4} dpa/s.
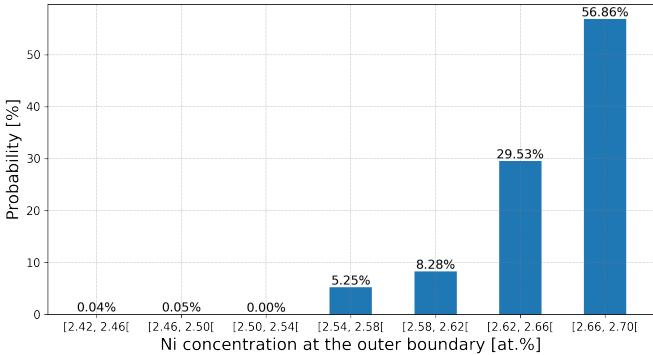
Figure 11: Calculated probabilities of the bulk Ni concentration at the outer boundary in Fe-Ni to be in the concentration intervals indicated by the x-axis. The effective nominal Ni concentration C_{Ni}^n is set to 2.70 at.%., the temperature is 400 °C, and the damage production rate is 9×10^{-4} dpa/s.

RIS model, C_{Ti}^{out} increases from 0.50 at.% ($r_l = 0.5\,\overline{r_l} = 3.5$ nm) to 0.58 at.% ($r_l = 3\,\overline{r_l} = 21$ nm).

According to the simulations, the Ti concentration field is highly heterogeneous within the Voronoi volume: the Ti concentration, C_{Ti}, tends to zero close to the dislocation loop, while it is higher than the nominal concentration away from the loop (near the outer boundary). The Ti atomic fraction at the outer boundary (C_{Ti}^{out}) depends on both the Voronoi volume and the loop radius. In the same way as in Fe-Ni, we investigated the variation of C_{Ti}^{out} with the loop radius and the Voronoi volume by performing simulations for a set of 36 combinations of the (Voronoi volume/dislocation loop radius) pair using both toroidal and disc-like models (i.e., in total 2×36 simulations). Fig. 14 highlights a large dispersion of C_{Ti}^{out}. If the toroidal RIS model is applied, C_{Ti}^{out} goes up to 0.61 at.% for a large loop ($r_l = 3\,\overline{r_l}$) in a small Voronoi volume

($v = 1 - 2\,\sigma$), while it is nearly equal to the nominal concentration (0.48 at.%) for a small loop ($r_l = 0.5\,\overline{r_l}$) in a big Voronoi volume ($v = 1 + 3\,\sigma$). The dispersion of C_{Ti}^{out} predicted by the disc-like RIS model is more significant. C_{Ti}^{out} varies from 0.48 at.% (for $r_l = 0.5\,\overline{r_l}$ and $v = 1 + 3\,\sigma$) to 0.72 at.% (for $r_l = 3\,\overline{r_l}$ and $v = 1 - 2\,\sigma$). Following the same statistical approach as the one performed for the Fe-Ni system, we compute the probability distribution of C_{Ti}^{out}, as shown in Fig. 15. In most cases (over 99% of probability), C_{Ti}^{out} is between 0.48 at.% and 0.58 at.% if the toroidal RIS model is used, and between 0.48 at.% and 0.62 at.% if the disc-like model is used. A value of C_{Ti}^{out} above 0.62 at.% is almost impossible, because the probabilities of having a pair equal to $(v, r_l) = (1 - 2\,\sigma, 3\,\overline{r_l})$ or $(1 - \sigma, 3\,\overline{r_l})$ is very small. Hence, in most cases, the increase of C_{Ti}^{out} resulting from the depletion in Ti at dislocation loops can go up to $+0.10$ at.% (over 20% of the nominal concentration) with the toroidal RIS model being used, and up to $+0.14$ at.% (over 30% of the nominal concentration) with the disc-like RIS model being used.

7.2. Distribution of the solute concentration in the APT volume

In the Fe-Ni system, the concentration of Ni away from the dislocation loops is not significantly affected by a RIS phenomenon. In worse cases, the relative change of the bulk Ni content is approximately 10%. On the other hand, in the Ni-Ti system, the simulations highlight a great dispersion of the Ti concentration away from the dislocation loops. As mentioned in Section 6, Ti concentrations measured in the eight APT specimens are very different from each other. This dispersion is certainly related to the Ti RIS and its variations with the dislocation loop radius and Voronoi volume. The volumes of APT specimens are all smaller than the average Voronoi volume: half of them (no. 1, 2, 5, 6, 7 in Table 3) are only about 1/6 of the average Voronoi volume. Therefore, Ti contents measured in these specimens correspond to local concentrations of partial volumes smaller than the average Voronoi volume. If a APT specimen is lifted in regions away from dislocation loops, it is very likely that the measured average Ti content is within the concentration range of C_{Ti}^{out}, which is predicted to be 0.48–0.58 at.% if the toroidal RIS model is applied, and 0.48–0.62 at.% if the disc-like model is used. If a APT specimen is lifted near a dislocation loop, the average Ti content of the specimen can be much lower than the nominal concentration (0.48 at.%), due to Ti depletion.

In order to simulate the dispersion of the Ti content measured by APT, we combine our post-treatment of the solute concentration field with a statistical simulation method as explained in Section 4.3. The volumes of APT specimens are not equal. We set the APT control cylinder volume to the minimum one, $V_{APT} = 9 \times 10^4$ nm³, and the associated radius to $r_{APT} = 30$ nm. Fig. 16 shows the resulting probability distribution of Ti contents measured in APT specimens of the Ni-Ti system. Relying on the simulation results given by the toroidal RIS model, in most
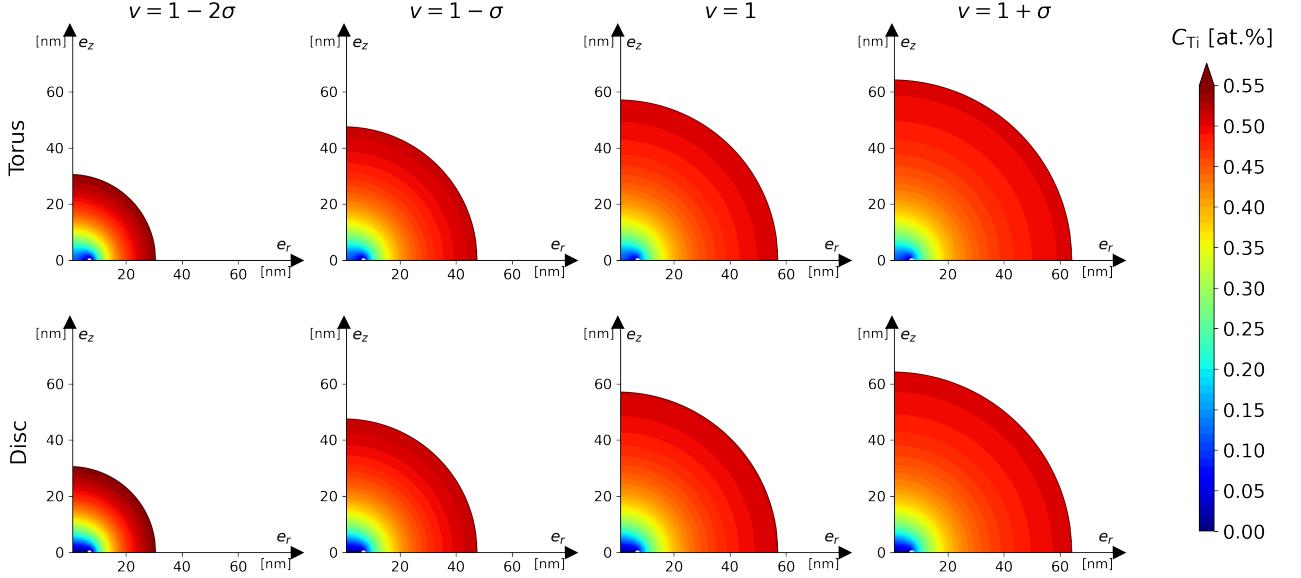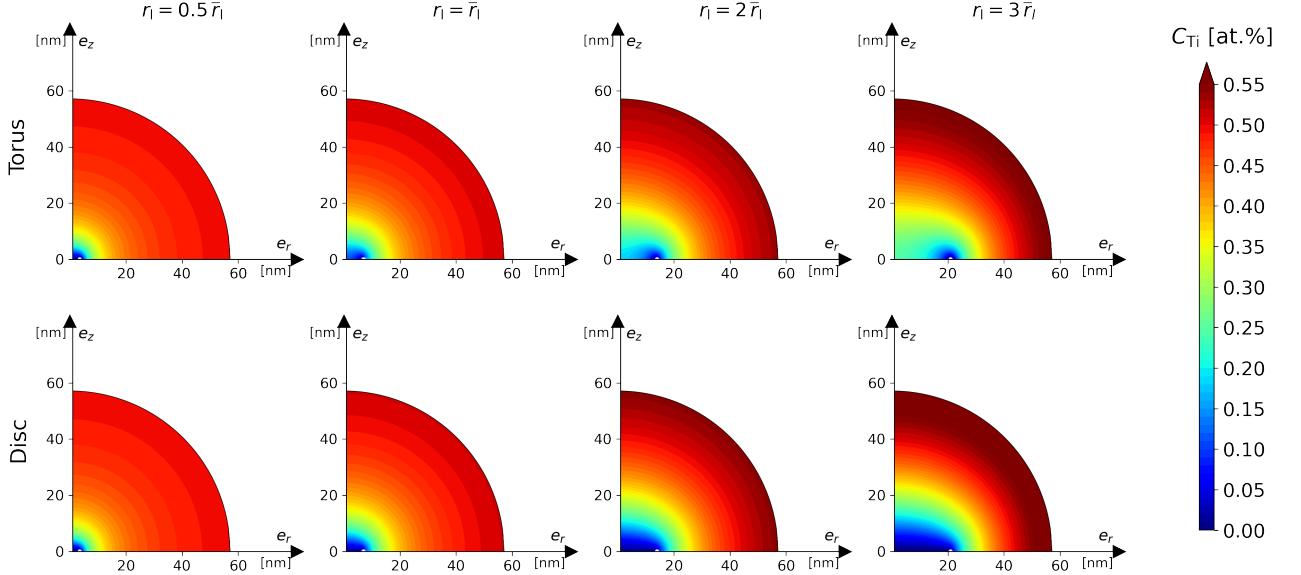
Figure 12: The Ti concentration field around a dislocation loop in Ni-Ti with toroidal (up) and disc-like (down) RIS regions for various Voronoi's volumes. $v = V_v/\overline{V_v}$ corresponds to the ratio between the Voronoi's volume (V_v) and the average one ($\overline{V_v}$). $\sigma = 0.42$ is the standard deviation of the Poisson-Voronoi distribution. The average Voronoi's volume is set to 7.7×10^5 nm^3 and the loop radius is set to its average value (7.0 nm). The effective nominal Ti concentration C_{Ti}^n is set to 0.48 at.%, the temperature is 450 °C, and the damage production rate is 8×10^{-5} dpa/s.


Figure 13: The Ti concentration field around a dislocation loop in Ni-Ti with toroidal (up) and disc-like (down) RIS regions for various loop radii. $\overline{r_l} = 7.0$ nm is the average loop radius. The Voronoi's volume is set to its average value (7.7×10^5 nm^3). The effective nominal Ti concentration C_{Ti}^n is set to 0.48 at.%, the temperature is 450 °C, and the damage production rate is 8×10^{-5} dpa/s.

cases, an average Ti atomic fraction measured by APT is between 0.33 at.% and 0.55 at.%, whereas using the results given by the disc-like model, the dispersion of the Ti concentration in the APT volume is larger: it varies from 0.29 at.% to 0.57 at.%.

7.3. Profile of RIS at dislocation loops

As presented in the previous section, a variation of the Voronoi volume hardly changes the Ni redistribution around a dislocation loop. Hence, we do not expect an effect of the Voronoi volume on the simulated APT profile. We then restrict our study to the effect of the dislocation loop radius. By relying on the simulation method pre-

15
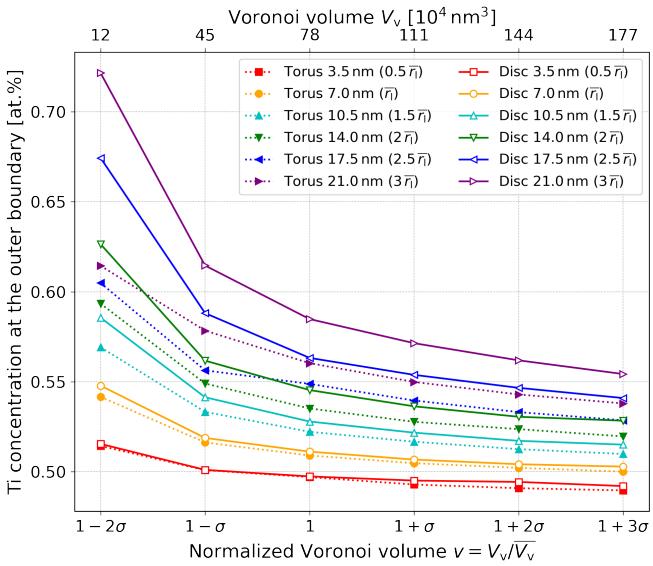
Figure 14: The distribution of the Ti concentration at the outer boundary in Ni-Ti obtained with different Voronoi volumes and dislocation loop radii, given by the toroidal and disc-like RIS models. $\overline{r_l} = 7.0$ nm is the average loop radius. The nominal Ti concentration C_{Ti}^n is set to 0.48 at.%, the temperature is $450\,°C$, and the damage production rate is 8×10^{-5} dpa/s.
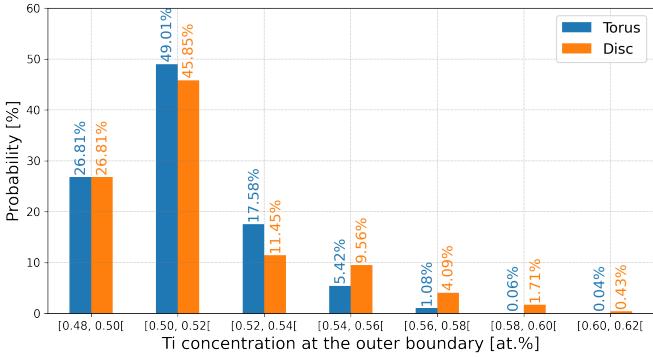
Figure 15: The probabilities for the Ti concentration at the outer boundary in Ni-Ti to be in different value ranges, given by the toroidal and disc-like RIS models. $\overline{r_l} = 7.0$ nm is the average loop radius. The nominal Ti concentration C_{Ti}^n is set to 0.48 at.%, the temperature is $450\,°C$, and the damage production rate is 8×10^{-5} dpa/s.

sented in section 4.3, we calculate 1D RIS profiles, for different values of the loop radius as shown in Fig. 17. In case the longitudinal direction of the control volume ($\boldsymbol{u}_{APT}$) is parallel to the loop's Burgers vector $\boldsymbol{b}_v$ (perpendicular to the dislocation habit plane), we observe in Fig. 17-(a) that the Ni RIS profile is a sharp peak centered on the dislocation loop center. On the other hand, in case $\boldsymbol{u}_{APT}$ is perpendicular to $\boldsymbol{b}_v$, we observe in Fig. 17-(b) the formation of multiple peaks. For $r_l = \overline{r_l}$, the RIS profile is a 'W'-shape profile. For $r_l = 2\,\overline{r_l}$ and $3\,\overline{r_l}$, the RIS profile have two peaks. Both of them are wider than the single peak profile represented in Fig. 17-(b).

In Fig. 18, we show that a change of the control volume

radius may lead to very different simulated RIS profiles. Since the variation of the Ni concentration basically occurs in a very local area near the dislocation loop (approximately 2 nm from the loop), a large control volume, as for example with a radius equal to 5 nm, cannot capture this local variation, and the corresponding simulated RIS profile is rather flat. On the contrary, a small control volume (e.g., the radius is 2 nm), which is sensitive to sharp variations of the local concentration, would lead to simulated RIS profiles with higher peaks. Let us emphasize that, even though the direction and the radius of the control volume are not physical parameters, they may have a strong impact on the simulated RIS profiles.

Opposite to what occurs in the Fe-Ni system, the variation of the Voronoi volume in the Ni-Ti system has a remarkable effect on the simulated RIS concentration profiles. We plot, in Fig. 19, the 1D-profile of Ti around an average dislocation loop obtained with different Voronoi's volumes. The Ti RIS profile has a shape of reverse peak due to the Ti depletion at the dislocation loop. The larger the Voronoi's volume, the wider the reverse peak. The RIS profile depends as well on the dislocation loop radius (cf. Fig. 20). The width of the reverse peak increases with the loop radius.

In the case where the longitudinal direction of the control volume is parallel to the loop's Burgers vector (Fig. 19-(a) and Fig. 20-(a)), the Ti RIS profiles are sharp inverse peaks. However, if the longitudinal direction of the control volume is perpendicular to the Burgers vector (Fig. 19-(b) and Fig. 20-(b)), the Ti profiles have a "basin" shape, especially for the profile of large loops (e.g., $r_l \geq 2\,\overline{r_l}$).

The 1D profiles for small loops ($r_l \leq \overline{r_l}$) given by the toroidal and disc-like RIS models are similar. For bigger loops (e.g., $r_l = 3\overline{r_l}$), the disc-like RIS model predicts a lower concentration at the position of loop center than that given by the toroidal model.

8. Discussion

8.1. Comparison between simulations and experiments

In this section, we discuss the comparison between the solute redistributions obtained from the simulations and the ones measured by APT. First, we analyse the APT RIS profiles. Since APT does not provide access to the radius and the local density of the dislocation loops, we compare the experimental profiles with a set of simulated RIS profiles obtained for a set of combinations of the Voronoi volume/loop radius pair. Besides, the habit plane of dislocation loops (or the direction of the Burger's vector) in both systems is unknown. Hence, we present simulated profiles for the two limiting cases: (i) the control cylinder volume is perpendicular and (ii) the control volume is parallel to the Burgers vector. In the Ni-Ti system, we present, as well, a detailed discussion on the dispersion of Ti content away from the dislocation loop.
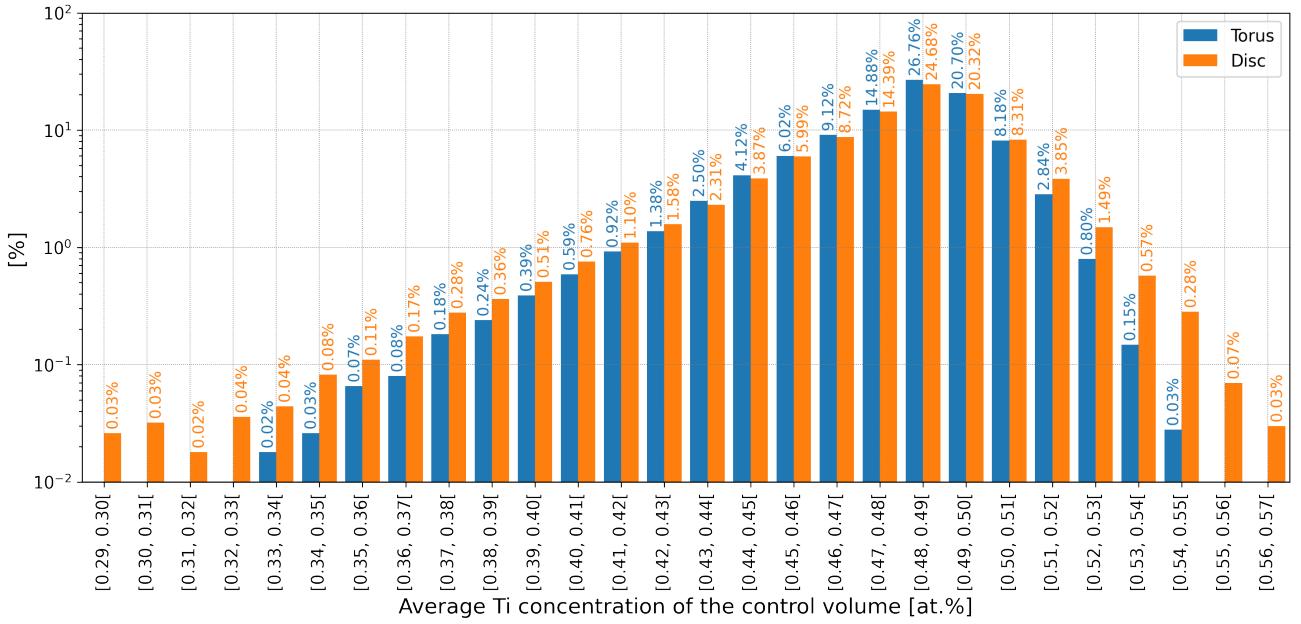
Figure 16: The density histograms of the average Ti concentration in the APT volume of Ni-Ti, given by the toroidal and disc-like RIS models. $\overline{r}_l = 7.0$ nm is the average loop radius. The nominal Ti concentration C_{Ti}^n is set to 0.48 at.%, the temperature is 450 °C, and the damage production rate is 8×10^{-5} dpa/s.

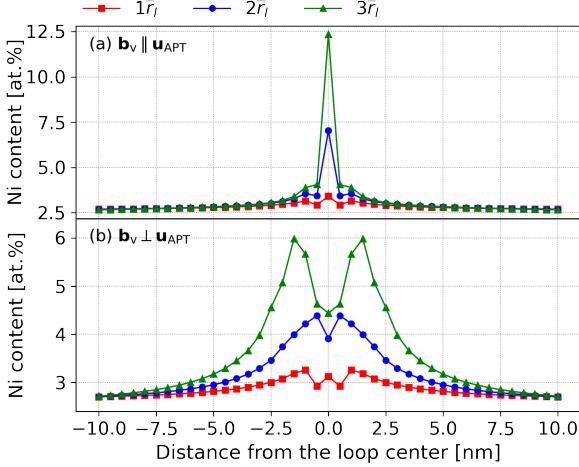Figure 17: The uni-dimensional Ni concentration profile across the dislocation loops in Fe-Ni for various loop radii ($r_l = \overline{r}_l$, $2\overline{r}_l$, $3\overline{r}_l$). The Voronoi volume is set to its average value. The radius of the cylindrical control volume is set to 3.5 nm. The longitudinal direction of the cylinder ($\boldsymbol{u}_{APT}$) is (a) parallel, (b) perpendicular to the Burgers vector of the edge dislocation loop ($\boldsymbol{b}_v$). The effective nominal Ni concentration C_{Ni}^n is set to 2.70 at.%., the temperature is 400 °C, and the damage production rate is 9×10^{-4} dpa/s.

Figure 18: The uni-dimensional Ni concentration profile across the dislocation loops in Fe-Ni for different control volume radii (2.0, 3.5, 5.0 nm). The Voronoi's volume is set to its average value. The loop radius is set to $2\overline{r}_l = 1.2$ nm. The longitudinal direction of the cylinder ($\boldsymbol{u}_{APT}$) is (a) parallel, or (b) perpendicular to the Burgers vector of the edge dislocation loop ($\boldsymbol{b}_v$). The effective nominal Ni concentration C_{Ni}^n is set to 2.70 at.%., the temperature is 400 °C, and the damage production rate is 9×10^{-4} dpa/s.

In Fig. 21, we compare the simulated RIS profile with three representative experimental profiles. The three experimental peaked profiles are all much wider and higher than the simulated ones. In particular, the maximum Ni atomic fraction of the profile of loop 9 is equal to 40 at.%, at the center of the loop. From our quantitative modeling of the Ni RIS dispersion, we may conclude that Ni segregation at dislocation loops is not a simple RIS phenomenon. The authors of Ref. [16] report that radiation-induced precipitation of metastable face-centered cubic phases (containing around 25 at.% Ni and 50 at.% Ni) may occur at dislocation loops in Fe-3.3Ni model alloys [17]. Most of
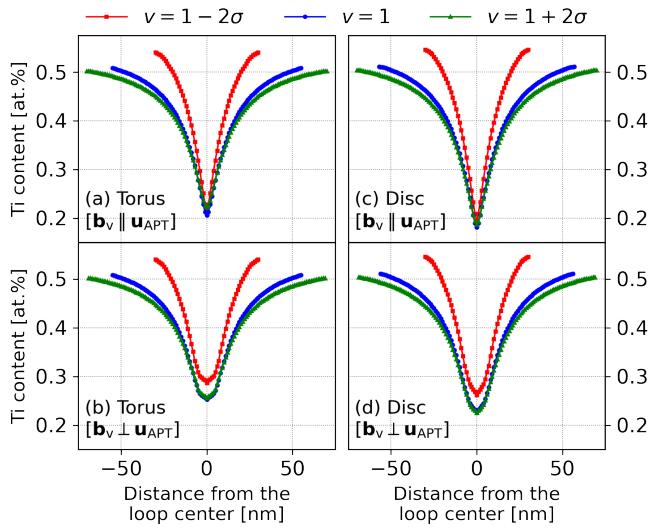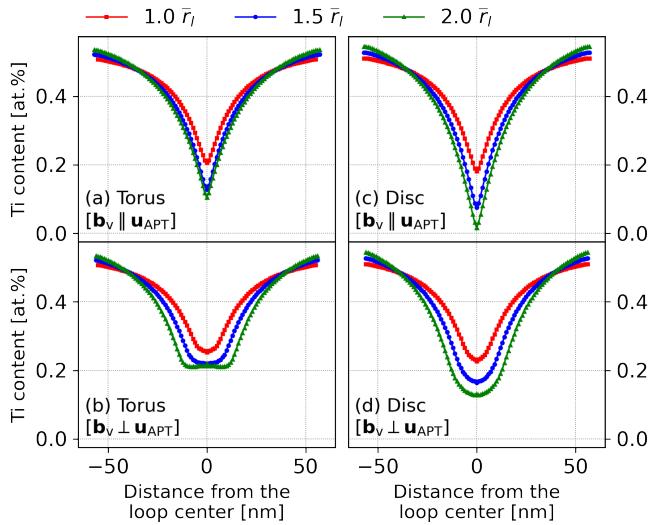
Figure 19: The 1D Ti concentration profile across the dislocation loops in Ni-Ti with toroidal (left) and disc-like (right) RIS regions for various Voronoi's volumes ($V_{\mathrm{v}}/\overline{V_{\mathrm{v}}} = 1 - 2\,\sigma, 1, 1 + 2\,\sigma$). The loop radius is set to its average value (7.0 nm). The radius of the cylindrical control volume is set to 15 nm. In (a) and (c), the longitudinal direction of the cylinder ($\boldsymbol{u}_{\mathrm{APT}}$) is parallel to the Burgers vector of the edge dislocation loop ($\boldsymbol{b}_{\mathrm{v}}$); in (b) and (d), $\boldsymbol{u}_{\mathrm{APT}}$ is perpendicular to $\boldsymbol{b}_{\mathrm{v}}$. The nominal Ti concentration $C_{\mathrm{Ti}}^{\mathrm{n}}$ is set to 0.48 at.%, the temperature is 450 °C, and the damage production rate is 8×10^{-5} dpa/s.

Figure 20: The 1D Ti concentration profile across the dislocation loops in Ni-Ti with toroidal (left) and disc-like (right) RIS regions for various loop radii ($r_{\mathrm{l}} = \overline{r_{\mathrm{l}}}, 1.5\,\overline{r_{\mathrm{l}}}, 2\,\overline{r_{\mathrm{l}}}$). The Voronoi's volume is set to its average value. The radius of the cylindrical control volume is set to 15 nm. In (a) and (c), the longitudinal direction of the cylinder ($\boldsymbol{u}_{\mathrm{APT}}$) is parallel to the Burgers vector of the edge dislocation loop ($\boldsymbol{b}_{\mathrm{v}}$); in (b) and (d), $\boldsymbol{u}_{\mathrm{APT}}$ is perpendicular to $\boldsymbol{b}_{\mathrm{v}}$. The nominal Ti concentration $C_{\mathrm{Ti}}^{\mathrm{n}}$ is set to 0.48 at.%, the temperature is 450 °C, and the damage production rate is 8×10^{-5} dpa/s.

the measured segregation profiles presented in Fig. 6 reach Ni atomic fractions above 25 at.%, up to 57 at.%. There-

fore, these Ni-rich clusters could be precipitates formed by a radiation-induced precipitation mechanism triggered by RIS of Ni at dislocation loops. In opposition to what has been observed at low radiation flux, clustering of Ni atoms in these Fe-Ni samples irradiated at higher flux does not proceed through the removal of dislocation loops. In order to confirm this radiation induced segregation-precipitation sequence, the crystallographic structure of these clusters needs to be analysed further, which goes beyond the scope of this paper.

In Fig. 22, we compare the simulated RIS profiles in the Ni-Ti system (from the toroidal model) to the two experimental profiles presented in Fig. 7. The shape and width of the reversed peak profile, as well as the Ti content at the center of the dislocation loop of the simulated profiles correspond well to those of the experimental profiles. The simulated profiles with $r_{\mathrm{l}} = \overline{r_{\mathrm{l}}}$ are in better agreement with the experimental profile than the one with $r_{\mathrm{l}} = 2\,\overline{r_{\mathrm{l}}}$. Hence, we may infer that the radii of loops 1 and 2 are close to the average one. Considering that the dislocation loop with an average radius results in very similar 1D concentration profiles given by the toroidal and disc-like models, the profile given by the disc-like model is also in good agreement with the experimental profile. Thus, the current experimental profiles do not allow us to identify whether the measured segregation regions are of toroidal or disc-like forms.

In the Ni-Ti system, the simulations have shown that the relative variation of the Ti content away from dislocation loops is significant. Fig. 16 shows a dispersion of $C_{\mathrm{Ti}}^{\mathrm{out}}$ between 0.33 at.% and 0.55 at.% as predicted by a toroidal RIS model and between 0.29 at.% and 0.57 at.% as predicted by a disc-like RIS model. The dispersion of the APT Ti content simulated by the disc-like model is in better agreement with the experimental one. However, experimentally, the dispersion is larger than the simulated one. The Ti atomic fraction in specimens 2, 3, 7 is higher than 0.57 at.%. The shift of Ti contents towards higher values than the simulated ones could be due to RIS of Ti at other PD sinks of the microstructure, as for example dislocation lines. Additional depleted zones of Ti around dislocation lines would slightly increase the effective nominal concentration of Ti within Voronoi volumes surrounding the dislocation loops. An increase of the Ti effective nominal concentration would increase the Ti content away from dislocation loops.

8.2. Comparison between Fe-Ni and Ni-Ti alloys

Thanks to the presented modeling investigation, we may provide reasons for the differences in RIS behaviors between the two alloys.

- Both the experimental measurement and the simulation agree on the RIS tendencies in these alloys. Ni is enriched at PD sinks in Fe-Ni, while Ti is depleted at PD sinks in Ni-Ti. These RIS tendencies are in
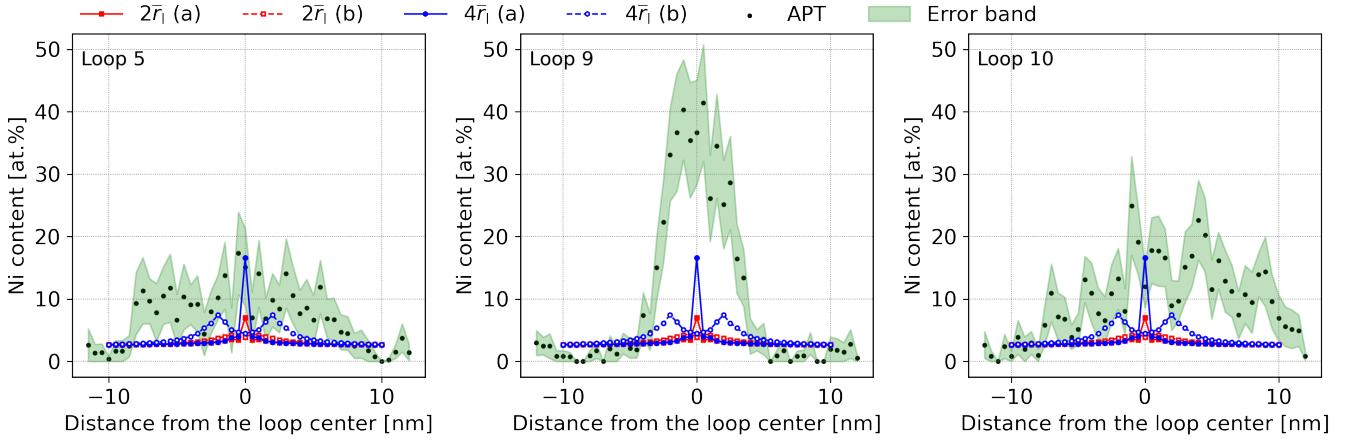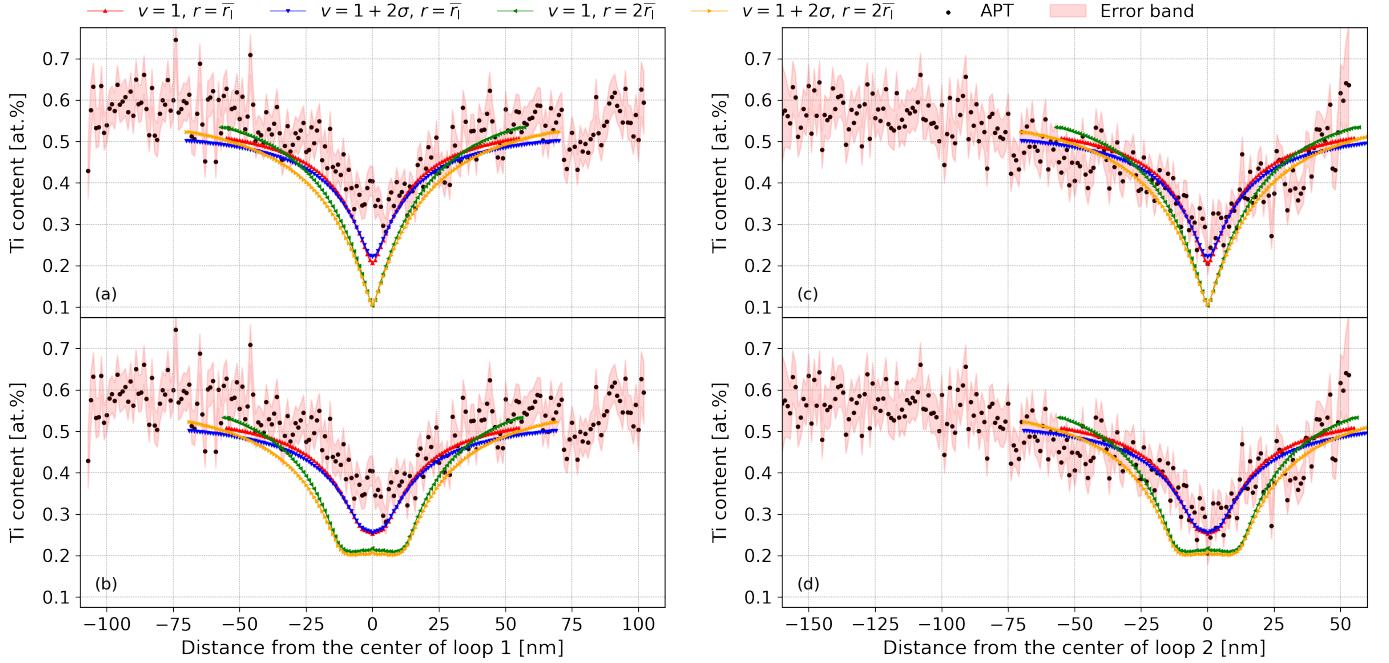
Figure 21: Comparison between the experimental and simulated RIS Ni 1D-profile in Fe-Ni. The simulation is performed with dislocation loops of radii $r_1 = 2\,\overline{r_1}$, $4\,\overline{r_1}$, and the Voronoi's volume set to its average value ($1.8 \times 10^4\,\text{nm}^3$). The radius of the cylindrical control volume is set to the experimental value of the control volume used in the APT analysis (3.5 nm). The longitudinal direction of the control volume is (a) parallel or (b) perpendicular to the Burgers vector of the dislocation loop.

Figure 22: Comparison between the experimental and simulated RIS Ni 1D-profile in Ni-Ti. The simulation is performed for different values of dislocation loop radii and Voronoi's volumes. The radius of the cylindrical control volume is set to the experimental radius of the control volume used in the APT analysis (15 nm). In (a) and (c), the longitudinal direction of the control volume is parallel to the Burgers vector of the dislocation loop. In (b) and (d), the longitudinal direction of the control volume is perpendicular to the Burgers vector of the dislocation loop. As presented in Fig. 7, the experimental profiles in (a) and (b) are associated to loop 1, while those in (c) and (d) are associated to loop 2.

line with previous studies of flux coupling in the Fe-Ni alloy [28] and in the Ni-Ti alloy [25]. According to these studies, Ni (in bcc Fe) and Ti (in fcc Ni) do not migrate via the SIA mechanism due to repulsion between these species and dumbbell-type SIAs. Therefore, in both alloys, only the vacancy mechanism contributes to RIS. In Ni-Ti, at the considered temperature (723 K), the Ti-vacancy flux coupling proceeds via the inverse-Kirkendall mechanism, e.g. Ti and vacancies move in opposite directions. Ti is depleted at sinks because its exchange frequency with vacancy is higher than the Ni-vacancy exchange frequencies. In Fe-Ni, the Ni-vacancy attraction is so high that a solute drag effect occurs at the investigated temperature (673 K), i.e., Ni and vacancies move in the same direction. This effect strongly depends on the varia-

tion of the vacancy-Fe exchange frequencies with the local concentration in Ni. Therefore, it is much more difficult to obtain a quantitative modeling of the flux couplings in Fe-Ni than those in Ni-Ti.

- According to Figs. 8 and 19, the effect of the Voronoi volume on solute redistribution in Ni-Ti is greater than that in Fe-Ni. This difference is related to the ratio between the average radius of the dislocation loop (r_l) and the average Voronoi's volume (r_{out} in Fig. 1). This ratio is equal to $\overline{r_l}/\overline{r_{out}} \sim 1/30$ in Fe-Ni, whereas it is much smaller in Ni-Ti: $\overline{r_l}/\overline{r_{out}} \sim 1/10$. If $r_l \ll r_{out}$, the amount of solute segregated at the dislocation loop is relatively small compared to the total amount of solute atoms belonging to the Voronoi's volume. This is a case where RIS depends little on the boundary conditions, in particular the radius of the Voronoi volume (r_{out}). If $r_l \sim r_{out}$, the dislocation loop is almost touching the surface of the Voronoi's volume, and the amount of solute segregated at the dislocation loop represents a significant part of the total amount of solute belonging to the Voronoi's volume. This is a case where RIS strongly depends on the outer radius, r_{out}. Therefore, the smaller ratio, $\overline{r_l}/\overline{r_{out}}$, explains why the solute redistribution in Ni-Ti is more sensitive to the size of the Voronoi's volume than in Fe-Ni. An effect of the volume of Voronoi on solute redistribution also means a significant variation of the bulk solute concentration with the local density of dislocation loops.

- As shown in Section 8.1, the agreement between the simulated and experimental RIS profiles in Ni-Ti is excellent, while the agreement in Fe-Ni is less satisfactory. In Fe-Ni, Ni is highly enriched at dislocation loops, while Ti is depleted at loops. A local enrichment of solute at sinks often leads to local supersaturations of the alloy and subsequent precipitation phenomena. Hence, in microstructure including solute-enriched defects, RIS rarely operates alone. A quantitative modeling of RIS is a necessary first step. In Ni-Ti, Ti is depleted at sinks. Therefore, a supersaturation in Ti may occur in the bulk only. It explains the very good agreement between the simulated RIS profile and the APT measured ones. Far from dislocations, the APT investigation did not reveal any Ti clustering phenomenon. Thus, the density of potential Ti clusters is very low. We may conclude that solute redistribution in Ni-Ti is mostly due to RIS of Ti at PD sinks.

8.3. Assumptions made in the present RIS model and their influence on the results

In this section, we discuss the major assumptions made in computing the solute redistribution profiles, and their potential impact on the results. This discussion should highlight the limitations and possible lines of improvements of the present approach.

- In the present model, we rely on the Voronoi's decomposition to model a non uniform spatial distribution of the dislocation loops. As a preliminary approach, we assume that the Voronoi's volume is a sphere and the dislocation loop center coincide with the center of the Voronoi's volume. This allows us to reduce the 3D diffusion problem into a 2D diffusion problem. In a realistic microstructure, Voronoi volumes are polyhedrons with arbitrary forms. A possible way to investigate the effect of the Voronoi's volume shape would be to solve the diffusion equation system [Eq. (19)] within an arbitrary polyhedron and compare the solute redistribution with the one obtained within a sphere of the same volume. However, solving the diffusion equation of an arbitrary polyhedron would require more CPU-consuming calculations. However, changing the shape of the Voronoi volume should not significantly modify the sink strength [66]. The potential magnitude of error is not large enough to justify the higher computational cost of a 3D calculation.

- The simulation method is restricted to a single dislocation loop in its Voronoi's volume. The surrounding environment, outside the Voronoi volume, is treated as a mean field where the solute concentration is assumed to be uniform. However, the effect of the neighboring loops on the RIS of a given loop may strongly deviate from a mean-field effect, especially because the dislocation loop with its elastic interaction field is a directional object. The calculation of RIS resulting from multiple dislocation loops treated explicitly is a complex 3D CPU-consuming problem. Besides, additional information is required, such as the distribution of the Voronoi volumes and the radii of the neighbouring loops. Here again, we expect the neighbouring effects to enhance the dispersion of the Ti concentration within the microstructure.

- The computation of the transport coefficients is based on the dilute limit approximation. This assumption is challenged in Fe-Ni because the Ni enrichment leads to a very high Ni content (up to 50 at.%) at the dislocation loop. One may perform kinetic Monte Carlo simulation to compute the transport coefficients, provided that the energy database of the point-defect migration barriers in a Ni-rich environment is available. Since the Ni-concentrated area is very small (limited to $\sim 1\,\text{nm}$ from the dislocation loop), we do not expect this possible concentration effect on the transport coefficients to significantly change the simulated RIS profile.

- Elastodiffusion is neglected in the present study. It was shown in Ref. [75] that, in pure Fe and Ni, elastodiffusion had a significant effect on the absorption bias of the cavities, while for a straight dislocation it leads to a relatively slight increase of the sink strength (within 25% at a conventional dislocation density,
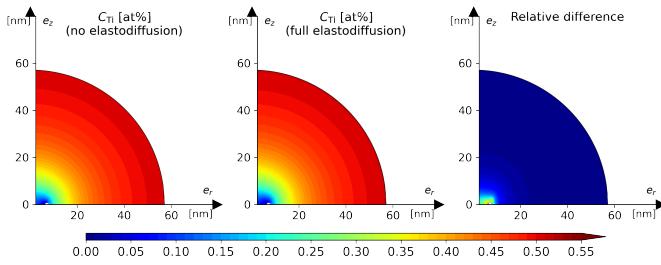
Figure 23: The Ti concentration fields around a dislocation loop in Ni-Ti obtained with and without considering the elastodiffusion; and the relative difference between these two concentration fields. The loop radius and the Voronoi's volume are set to their average values, respectively. The effective nominal Ti concentration C_{Ti}^{n} is set to 0.48 at.%, the temperature is $450\,°C$, and the damage production rate is 8×10^{-5} dpa/s.
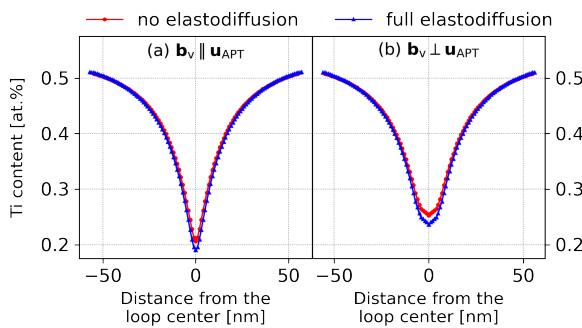

Figure 24: The uni-dimensional Ti concentration profiles across the dislocation loop in Ni-Ti obtained with and without considering the elastodiffusion. The loop radius and the Voronoi's volume are set to their average values, respectively. The longitudinal direction of the cylinder ($\boldsymbol{u}_{APT}$) is (a) parallel, or (b) perpendicular to the Burgers vector of the edge dislocation loop ($\boldsymbol{b}_{v}$). The effective nominal Ti concentration C_{Ti}^{n} is set to 0.48 at.%, the temperature is $450\,°C$, and the damage production rate is 8×10^{-5} dpa/s.

e.g., 10^{14}–$10^{15}\,\mathrm{m}^{-2}$) and a small decrease of the sink bias (by $\sim 10\%$). Currently, there is no study about the elastodiffusion effect on the PD absorption by dislocation loops in Fe or Ni. We assume the elastodiffusion effect on the dislocation loops to be similar to the one on the straight dislocation. Therefore, the elastodiffusion may slightly increase the sink strength of the dislocation loops, leading to higher PD fluxes toward the loops. To investigate the influence of the elastodiffusion on the solute redistribution, we perform a RIS simulation for a dislocation loop of average radius within an average Voronoi volume in Ni-Ti including the effect of the elastodiffusion; then, we compare this simulation result to the one without elastodiffusion. The elastic dipoles of PDs and Ti atoms at the saddle-point configurations can be found in Supplementary Material. The comparison of the solute concentration fields is plotted in Fig. 23 and the one of the 1D RIS profiles is presented in Fig. 24. Elastodiffusion modifies the Ti concentration field close to the loop (within 5 nm from the loop center). How-

ever, the area where the relative difference is higher than 10% corresponds only to a small volume ($< 1\%$ of the entire simulation volume). Therefore, elastodiffusion hardly changes the 1D RIS profile. The 1D profiles obtained with and without elastodiffusion are nearly the same in terms of the accuracy of experimental measurements by APT. We conclude that the elastodiffusion has very small effects on the RIS in Ni-Ti, which justifies our assumption.

8.4. Our prescriptions for future RIS experimental studies

- As presented in Fig. 18, the 1D RIS profile measured by APT depends on the post-treatment parameters, such as the shape and the size of the control volume used in the analysis. The APT measurement is all the more sensitive to the post-treatment parameters as the RIS profile is sharp. Therefore, when comparing two experimental RIS profiles, it is essential to ensure that the same post-treatment parameters of the solute concentration field are used. Compared to the 1D RIS profile, the bulk solute concentration away from dislocation loops is a more reliable data, because this concentration should be much less sensitive to the post-treatment parameters. This bulk concentration provides direct insight on the overall amount of RIS. In case of solute enrichment, the lower the solute concentration in the bulk area, the higher the solute enrichment at sinks. On the other hand, in case of solute depletion, the higher the bulk solute concentration, the higher the depletion at sinks.

- A RIS study is only complete if its statistical dispersion is accounted for. Unless the microstructure is made of a single population of defects homogeneously distributed in space, and with a peaked distribution in size, a single RIS profile is not representative of the RIS distribution. In alloys with sizes of defects of the same order of magnitude than the Voronoi's volume, the bulk concentration is a statistical quantity as well.

9. Conclusions

From a systematic APT characterization of solute redistribution in dilute Fe-Ni and Ni-Ti irradiated alloys, we highlight the fluctuating nature of the local solute concentration resulting from a RIS mechanism. By relying on a full characterization of the microstructure by TEM and an *ab-initio* based modeling of RIS, we show that the dispersion of RIS is related to the dispersion of the microstructure together with the nanoscale resolution of the characterization technique. To simulate the dispersion of the microstructure, we introduce randomly distributed Voronoi's spherical volumes, each containing a single dislocation loop. The radius of the loop is sampled after an analytical distribution function adjusted to reproduce the experimental distribution in size of dislocation loops measured by TEM. From *ab initio* jump frequencies and

elastic dipoles of lattice point defects, we compute solute-point defect flux couplings with respect to the local composition and lattice strain generated by the dislocation loop. The steady state solution of the corresponding diffusion/reaction equation is obtained under the constraint of the solute conservation within the Voronoi's volume. The concentration of point defects at the surface of the Voronoi's volume is deduced from the steady state solution of a macroscopic mean field rate theory accounting for the creation and recombination reactions of point defects, and their average elimination rate at point defect sinks of the microstructure (including the dislocation loop population).

From the comparison between the simulations and the measured solute redistribution, we may conclude that *ab initio* based simulations of RIS have become quantitative simulation methods, as long as the solute redistribution is solely due to RIS, the elastic interactions, and the microstructure dispersion are taken into account. In systems where point defect sinks are depleted in solute such as in the Ni-Ti alloy, RIS is likely to operate alone. In this system, the simulated RIS profiles are in very good agreement with APT profiles. The distribution of bulk solute contents extracted from the solute content of various APT specimens is correctly reproduced, though the set of specimens is too small to be representative of the bulk solute concentration distribution. In Fe-Ni, the identification of discrepancies between simulated RIS profiles and the measured ones provides a signature of additional operating mechanisms of solute redistribution, such as radiation-induced precipitation. We highlight the strong impact of the resolution and the direction of the APT control volume on the shape of RIS profiles. Furthermore, we demonstrate that the specific microstructure of the irradiated Ni-Ti generates fluctuations of the Ti local content up to the APT specimen scale.

Thanks to the comparison between the Fe-Ni and Ni-Ti alloys, we obtain criteria on the solute redistribution sensitivity to the local microstructure and the resolution of the experimental characterization techniques. An increase of the radius of dislocation loops significantly increases RIS. Therefore, a large variation of this radius will yield a large dispersion of RIS. Besides, we expect an effect of the local density fluctuations of point defect sinks, when the average Voronoi's volume occupied by a single defect sink is slightly bigger than the volume of the defect. The bulk solute concentration far from sinks has then a large distribution that is sensitive to the dispersion of the microstructure, the resolution of the characterization technique, and the details of the elastic interactions generated by the defect sink. For instance, the faulted nature of the dislocation loop increases the width of the solute dispersion distribution by 50 %.

To conclude, we would like to emphasize that a full characterization of a nanoscale solute redistribution by means of atomic scale characterization techniques requires a statistical approach. The fluctuations of the measured solute content in volumes up to the scale of a APT specimen are related to the physical mechanism controlling the solute redistribution, but also to the dispersion of the microstructure together with the resolution of the characterization technique.

References

[1] T. R. Anthony, R. E. Hanneman, Non-equilibrium segregation of impurities in quenched dilute alloys, Scr. Metall. 2 (11) (1968) 611–614. doi:10.1016/0036-9748(68)90145-2.

[2] P. R. Okamoto, H. Wiedersich, Segregation of alloying elements to free surfaces during irradiation, J. Nucl. Mater. 53 (C) (1974) 336–345. doi:10.1016/0022-3115(74)90267-0.

[3] K. C. Russell, Phase stability under irradiation, Prog. Mater. Sci. 28 (3-4) (1984) 229–434. doi:10.1016/0079-6425(84)90001-X.

[4] A. J. Ardell, P. Bellon, Radiation-induced solute segregation in metallic alloys, Curr. Opin. Solid State Mater. Sci. 20 (3) (2016) 115–139. doi:10.1016/j.cossms.2015.11.001.
URL http://dx.doi.org/10.1016/j.cossms.2015.11.001

[5] M. Nastar, F. Soisson, Radiation-induced segregation, Vol. 1, Elsevier Inc., 2020. doi:10.1016/B978-0-12-803581-8.00668-8.
URL http://dx.doi.org/10.1016/B978-0-12-803581-8.00668-8

[6] M. Lee, G. Kim, Y. Jung, S. Ahn, Radiation-induced swelling and precipitation in fe++ ion-irradiated ferritic/martensitic steels, Journal of Nuclear Materials (2021) 153137 doi:https://doi.org/10.1016/j.jnucmat.2021.153137.
URL https://www.sciencedirect.com/science/article/pii/S0022311521003603

[7] G. S. Was, Fundamentals of Radiation Materials Science, Springer, Berlin, Heidelberg, 2007.

[8] S. J. Zinkle, G. S. Was, Materials challenges in nuclear energy, Acta Mater. 61 (3) (2013) 735–758. doi:10.1016/j.actamat.2012.11.004.
URL http://dx.doi.org/10.1016/j.actamat.2012.11.004

[9] S. M. Bruemmer, E. P. Simonen, P. M. Scott, P. L. Andresen, G. S. Was, J. L. Nelson, Radiation-induced material changes and susceptibility to intergranular failure of light-water-reactor core internals, J. Nucl. Mater. 274 (3) (1999) 299–314. doi:10.1016/S0022-3115(99)00075-6.

[10] M. K. Miller, K. F. Russell, Embrittlement of RPV steels: An atom probe tomography perspective, J. Nucl. Mater. 371 (1-3) (2007) 145–160. doi:10.1016/j.jnucmat.2007.05.003.

[11] A. Barbu, A. J. Ardell, Irradiation-induced precipitation in NiSi alloys, Scr. Metall. 9 (11) (1975) 1233–1237. `doi:10.1016/0036-9748(75)90415-9`.

[12] E. Wakai, A. Hishinuma, Y. Kato, H. Yano, S. Takaki, K. Abiko, Radiation-induced α' phase formation on dislocation loops in fe-cr alloys during electron irradiation, Journal de Physique IV 05-C7 (1995) 277 – 286.

[13] M. K. Miller, K. A. Powers, R. K. Nanstad, P. Efsing, Atom probe tomography characterizations of high nickel, low copper surveillance RPV welds irradiated to high fluences, J. Nucl. Mater. 437 (1-3) (2013) 107–115. `doi:10.1016/j.jnucmat.2013.01.312`.
URL `http://dx.doi.org/10.1016/j.jnucmat.2013.01.312`

[14] P. D. Styman, J. M. Hyde, D. Parfitt, K. Wilford, M. G. Burke, C. A. English, P. Efsing, Post-irradiation annealing of Ni-Mn-Si-enriched clusters in a neutron-irradiated RPV steel weld using Atom Probe Tomography, J. Nucl. Mater. 459 (2015) 127–134. `doi:10.1016/j.jnucmat.2015.01.027`.
URL `http://dx.doi.org/10.1016/j.jnucmat.2015.01.027`

[15] N. Castin, G. Bonny, A. Bakaev, F. Bergner, C. Domain, J. Hyde, L. Messina, B. Radiguet, L. Malerba, The dominant mechanisms for the formation of solute-rich clusters in low-Cu steels under irradiation, Mater. Today Energy 17 (2020) 100472. `doi:10.1016/j.mtener.2020.100472`.
URL `https://linkinghub.elsevier.com/retrieve/pii/S2468606920300915`

[16] L. T. Belkacemi, E. Meslin, B. Décamps, B. Radiguet, J. Henry, Radiation-induced bcc-fcc phase transformation in a Fe3%Ni alloy, Acta Materialia 161 (2018) 61 – 72. `doi:https://doi.org/10.1016/j.actamat.2018.08.031`.
URL `http://www.sciencedirect.com/science/article/pii/S1359645418306682`

[17] M. Nastar, L. T. Belkacemi, E. Meslin, M. Loyer-Prost, Thermodynamic model for lattice point defect-mediated semi-coherent precipitation in alloys, Communications Materials 2 (1) (2021) 32. `doi:10.1038/s43246-021-00136-z`.
URL `https://doi.org/10.1038/s43246-021-00136-z`

[18] G. S. Was, J. P. Wharry, B. Frisbie, B. D. Wirth, D. Morgan, J. D. Tucker, T. R. Allen, Assessment of radiation-induced segregation mechanisms in austenitic and ferritic–martensitic alloys, Journal of Nuclear Materials 411 (1-3) (2011) 41–50. `doi:10.1016/j.jnucmat.2011.01.031`.
URL `http://dx.doi.org/10.1016/j.jnucmat.2011.01.031https://linkinghub.elsevier.com/retrieve/pii/S0022311511000547`

[19] C. M. Barr, G. A. Vetterick, K. A. Unocic, K. Hattar, X.-M. Bai, M. L. Taheri, Anisotropic radiation-induced segregation in 316L austenitic stainless steel with grain boundary character, Acta Materialia 67 (2014) 145–155. `doi:10.1016/j.actamat.2013.11.060`.
URL `https://linkinghub.elsevier.com/retrieve/pii/S135964541300918X`

[20] C. Lu, L. Niu, N. Chen, K. Jin, T. Yang, P. Xiu, Y. Zhang, F. Gao, H. Bei, S. Shi, M.-R. He, I. M. Robertson, W. J. Weber, L. Wang, Enhancing radiation tolerance by controlling defect mobility and migration pathways in multicomponent single-phase alloys, Nature Communications 7 (1) (2016) 13564. `doi:10.1038/ncomms13564`.
URL `http://www.nature.com/articles/ncomms13564`

[21] K. Ma, B. Décamps, A. Fraczkiewicz, F. Prima, M. Loyer-Prost, Drastic influence of micro-alloying on Frank loop nature in Ni and Ni-based model alloys, Mater. Res. Lett. 8 (5) (2020) 201–207. `doi:10.1080/21663831.2020.1741042`.
URL `https://www.tandfonline.com/doi/full/10.1080/21663831.2020.1741042`

[22] P. Yvon (Ed.), Structural Materials for Generation IV Nuclear Reactors, 1st Edition, Woodhead Publishing, Cambridge, United Kingdom, 2016.
URL `https://www.elsevier.com/books/structural-materials-for-generation-iv-nuclear-reactors/yvon/978-0-08-100906-2`

[23] L. Belkacemi, E. Meslin, J.-P. Crocombette, B. Radiguet, F. Leprêtre, B. Décamps, Striking effect of solute elements (mn, ni) on radiation-induced segregation/precipitation in iron-based model alloys, Journal of Nuclear Materials 548 (2021) 152807. `doi:https://doi.org/10.1016/j.jnucmat.2021.152807`.
URL `https://www.sciencedirect.com/science/article/pii/S0022311521000301`

[24] L. Belkacemi, E. Meslin, B. Décamps, J.-P. Crocombette, O. Tissot, T. Vandenberghe, P. Desgardin, T. Sauvage, C. Berthier, Role of displacement cascades in ni clustering in a ferritic fe-3.3% at ni model alloy: Comparison of heavy and light particle irradiations, Scripta Materialia 188 (2020) 169–173. `doi:https://doi.org/10.1016/j.scriptamat.2020.07.031`.
URL `https://www.sciencedirect.com/science/article/pii/S1359646220304838`

[25] E. Toijer, L. Messina, C. Domain, J. Vidal, C. S. Becquart, P. Olsson, Solute-point defect interactions, coupled diffusion, and radiation-induced segregation in fcc nickel, Physical Review Materials 5 (1) (2021) 013602. `doi:10.1103/PhysRevMaterials.5.013602`.
URL `https://link.aps.org/doi/10.1103/PhysRevMaterials.5.013602`

[26] D. R. Trinkle, Automatic numerical evaluation of vacancy-mediated transport for arbitrary crystals: Onsager coefficients in the dilute limit using a Green function approach, Philosophical Magazine 97 (28) (2017) 2514–2563. `doi:10.1080/14786435.2017.1340685`.
URL `https://doi.org/10.1080/14786435.2017.1340685`

[27] T. Schuler, L. Messina, M. Nastar, KineCluE: A kinetic cluster expansion code to compute transport coefficients beyond the dilute limit, Comput. Mater. Sci. 172 (May 2019) (2020) 109191. `doi:10.1016/j.commatsci.2019.109191`.
URL `https://doi.org/10.1016/j.commatsci.2019.109191https://linkinghub.elsevier.com/retrieve/pii/S0927025619304902`

[28] L. Messina, M. Nastar, T. Garnier, C. Domain, P. Olsson, Exact ab initio transport coefficients in bcc Fe–X (X = Cr, Cu, Mn, Ni, P, Si) dilute alloys, Phys. Rev. B 90 (10) (2014) 104203. `doi:10.1103/PhysRevB.90.104203`.
URL `https://link.aps.org/doi/10.1103/PhysRevB.90.104203`

[29] T. Schuler, M. Nastar, Transport properties of dilute Fe(X) solid solutions (X = C, N, O), Phys. Rev. B 93 (22) (2016) 224101. `doi:10.1103/PhysRevB.93.224101`.
URL `https://link.aps.org/doi/10.1103/PhysRevB.93.224101`

[30] T. Schuler, P. Bellon, D. R. Trinkle, R. S. Averback, Modeling the long-term evolution of dilute solid solutions in the presence of vacancy fluxes, Phys. Rev. Mater. 2 (7) (2018) 073605. `doi:10.1103/PhysRevMaterials.2.073605`.
URL `https://link.aps.org/doi/10.1103/PhysRevMaterials.2.073605`

[31] L. Messina, T. Schuler, M. Nastar, M.-C. Marinica, P. Olsson, Solute diffusion by self-interstitial defects and radiation-induced segregation in ferritic Fe–X (X=Cr, Cu, Mn, Ni, P, Si) dilute alloys, Acta Materialia 191 (2020) 166–185. `doi:10.1016/j.actamat.2020.03.038`.
URL `https://linkinghub.elsevier.com/retrieve/pii/S1359645420302251`

[32] L. Huang, M. Nastar, T. Schuler, L. Messina, Multiscale modeling of the effects of temperature, radiation flux, and sink strength on point-defect and solute redistribution in dilute Fe-based alloys, Physical Review Materials 5 (3) (2021) 033605. `doi:10.1103/PhysRevMaterials.5.033605`.
URL `https://link.aps.org/doi/10.1103/PhysRevMaterials.5.033605`

[33] T. Garnier, V. R. Manga, D. R. Trinkle, M. Nastar, P. Bellon, Stress-induced anisotropic diffusion in alloys: Complex Si solute flow near a dislocation core in Ni, Phys. Rev. B 88 (13) (2013) 134108. `doi:10.1103/PhysRevB.88.134108`.
URL `https://link.aps.org/doi/10.1103/PhysRevB.88.`

134108

[34] T. Garnier, Z. Li, M. Nastar, P. Bellon, D. R. Trinkle, Calculation of strain effects on vacancy-mediated diffusion of impurities in fcc structures: General approach and application to $ni_{1-x}si_x$, Phys. Rev. B 90 (2014) 184301. doi:10.1103/PhysRevB.90.184301.
URL https://link.aps.org/doi/10.1103/PhysRevB.90.184301

[35] Z. Li, D. R. Trinkle, Mesoscale modeling of vacancy-mediated Si segregation near an edge dislocation in Ni under irradiation, Phys. Rev. B 95 (14) (2017) 144107. doi:10.1103/PhysRevB.95.144107.
URL http://link.aps.org/doi/10.1103/PhysRevB.95.144107

[36] L. Thuinet, H. Rouchette, A. Legris, 3D phase-field modelling of dislocation loop sink strengths, J. Nucl. Mater. 483 (2017) 62–81. doi:10.1016/j.jnucmat.2016.10.041.
URL http://dx.doi.org/10.1016/j.jnucmat.2016.10.041

[37] J. P. Hirth, J. Lothe, T. Mura, Theory of Dislocations (2nd ed.), J. Appl. Mech. 50 (2) (1983) 476–477. doi:10.1115/1.3167075.
URL https://asmedigitalcollection.asme.org/appliedmechanics/article/50/2/476/389516/Theory-of-Dislocations-2nd-ed

[38] T. Jourdan, Influence of dislocation and dislocation loop biases on microstructures simulated by rate equation cluster dynamics, J. Nucl. Mater. 467 (2015) 286–301. doi:10.1016/j.jnucmat.2015.09.046.
URL http://dx.doi.org/10.1016/j.jnucmat.2015.09.046

[39] D. Carpentier, T. Jourdan, P. Terrier, M. Athènes, Y. Le Bouar, Effect of sink strength dispersion on cluster size distributions simulated by cluster dynamics, Journal of Nuclear Materials 533 (2020) 152068. doi:10.1016/j.jnucmat.2020.152068.
URL https://linkinghub.elsevier.com/retrieve/pii/S0022311519312796

[40] M. Nastar, V. Y. Dobretsov, G. Martin, Self-consistent formulation of configurational kinetics close to equilibrium: The phenomenological coefficients for diffusion in crystalline solids, Philos. Mag. A 80 (1) (2000) 155–184. doi:10.1080/01418610008212047.

[41] M. Nastar, A mean field theory for diffusion in a dilute multi-component alloy: A new model for the effect of solutes on self-diffusion, Philos. Mag. 85 (32) (2005) 3767–3794. doi:10.1080/14786430500228390.

[42] J. Biersack, L. Haggmark, A Monte Carlo computer program for the transport of energetic ions in amorphous targets, Nucl. Instruments Methods 174 (1-2) (1980) 257–269. doi:10.1016/0029-554X(80)90440-1.
URL https://linkinghub.elsevier.com/retrieve/pii/0029554X80904401

[43] G. H. Kinchin, R. S. Pease, The Displacement of Atoms in Solids by Radiation, Reports on Progress in Physics 18 (1) (1955) 1–51. doi:10.1088/0034-4885/18/1/301.
URL https://doi.org/10.1088%2F0034-4885%2F18%2F1%2F301

[44] K. Ma, B. Décamps, A. Fraczkiewicz, T. Jourdan, F. Prima, M. Loyer-Prost, Free surface impact on radiation damage in pure nickel by in-situ self-ion irradiation: can it be avoided?, Acta Materialia 212 (2021) 116874. doi:10.1016/j.actamat.2021.116874.
URL https://doi.org/10.1016/j.actamat.2021.116874

[45] S. Zinkle, L. Snead, Opportunities and limitations for ion beams in radiation effects studies: Bridging critical gaps between charged particle and neutron irradiations, Scripta Materialia 143 (2018) 154–160. doi:10.1016/j.scriptamat.2017.06.041.
URL https://doi.org/10.1016/j.scriptamat.2017.06.041

[46] B. Horváth, R. Schäublin, Y. Dai, Flash electropolishing of tem lamellas of irradiated tungsten, Nuclear Instruments and Methods in Physics Research Section B: Beam Interactions with Materials and Atoms 449 (2019) 29–34.

[47] D. B. Williams, C. B. Carter, Transmission Electron Microscopy: A Textbook for Materials Science, 2nd Edition, Springer US, 2009.
URL //www.springer.com/gp/book/9780387765006

[48] L. Onsager, RECIPROCAL RELATIONS IN IRREVERSIBLE PROCESSES. I., Phys. Rev. 37 (1931) 405–426. doi:10.1103/PhysRev.37.405.

[49] L. Onsager, RECIPROCAL RELATIONS IN IRREVERSIBLE PROCESSES. II., Phys. Rev. 38 (1931) 2265–2279. doi:10.1103/PhysRev.38.2265.

[50] F. Ducastelle, Phase stability in alloys, North Holland, Amsterdam, 1991.

[51] T. Schuler, D. R. Trinkle, P. Bellon, R. Averback, Design principles for radiation-resistant solid solutions, Phys. Rev. B 95 (17) (2017). doi:10.1103/PhysRevB.95.174102.

[52] E. Clouet, C. Varvenne, T. Jourdan, Elastic modeling of point-defects and their interaction, Comput. Mater. Sci. 147 (2018) 49–63. arXiv:1802.04062, doi:10.1016/j.commatsci.2018.01.053.
URL https://doi.org/10.1016/j.commatsci.2018.01.053

[53] J. Weertman, The Peach–Koehler equation for the force on a dislocation modified for hydrostatic pressure, Philos. Mag. A J. Theor. Exp. Appl. Phys. 11 (114) (1965) 1217–1223. doi:10.1080/14786436508224930.
URL https://www.tandfonline.com/doi/full/10.1080/14786436508224930

[54] J. Lothe, J. P. Hirth, Dislocation Climb Forces, J. Appl. Phys. 38 (2) (1967) 845–848. doi:10.1063/1.1709423.
URL http://aip.scitation.org/doi/10.1063/1.1709423

[55] M. Nastar, F. Soisson, Radiation-induced segregation, Vol. 1, Elsevier Inc., 2012. doi:10.1016/B978-0-08-056033-5.00035-5.
URL http://dx.doi.org/10.1016/B978-0-08-056033-5.00035-5

[56] L. Huang, T. Schuler, M. Nastar, Atomic-scale modeling of the thermodynamic and kinetic properties of dilute alloys driven by forced atomic relocations, Phys. Rev. B 100 (2019) 224103. doi:10.1103/PhysRevB.100.224103.

[57] C. Lu, T. Yang, K. Jin, N. Gao, P. Xiu, Y. Zhang, F. Gao, H. Bei, W. J. Weber, K. Sun, Y. Dong, L. Wang, Radiation-induced segregation on defect clusters in single-phase concentrated solid-solution alloys, Acta Materialia 127 (2017) 98–107. doi:10.1016/j.actamat.2017.01.019.
URL http://dx.doi.org/10.1016/j.actamat.2017.01.019https://linkinghub.elsevier.com/retrieve/pii/S1359645417300290

[58] A. Seeger, U. Gösele, Steady-state diffusion of point defects to dislocation loops, Phys. Lett. A 61 (6) (1977) 423–425. doi:10.1016/0375-9601(77)90355-3.

[59] C. Woo, W. Liu, M. Wuschke, A finite-difference calculation of point defect migration into a dislocation loop (1979).
URL https://inis.iaea.org/search/search.aspx?orig_q=RN:11558103

[60] R. Bullough, M. Wood, D. Wells, J. Willis, THE INTERACTION ENERGY BETWEEN INTERSTITIAL ATOMS AND DISLOCATIONS AND ITS RELEVANCE TO IRRADIATION DAMAGE PROCESSES, in: Dislocation Modelling of Physical Systems, Elsevier, 1981, pp. 116–141. doi:10.1016/B978-0-08-026724-1.50017-0.
URL https://linkinghub.elsevier.com/retrieve/pii/B9780080267241500170

[61] W. Coghlan, M. Yoo, RADIUS DEPENDENCE OF THE SINK STRENGTH OF A DISLOCATION LOOP, in: Dislocation Modelling of Physical Systems, Elsevier, 1981, pp. 152–157. doi:10.1016/B978-0-08-026724-1.50020-0.
URL https://linkinghub.elsevier.com/retrieve/pii/B9780080267241500200

[62] V. I. Dubinko, A. S. Abyzov, A. A. Turkin, Numerical evaluation of the dislocation loop bias, J. Nucl. Mater. 336 (1) (2005) 11–21. doi:10.1016/j.jnucmat.2004.07.034.

[63] W. G. Wolfer, The Dislocation Bias, Journal of Computer-Aided Materials Design 14 (3) (2007) 403–417. doi:10.1007/s10820-007-9051-3.
URL http://link.springer.com/10.1007/s10820-007-9051-3

24

[64] H. Rauh, D. Simon, On the diffusion process of point defects in the stress field of edge dislocations, Phys. Status Solidi 46 (2) (1978) 499–510. `doi:10.1002/pssa.2210460213`.

[65] F. A. Nichols, On the estimation of sink-absorption terms in reaction-rate-theory analysis of radiation damage, J. Nucl. Mater. 75 (1) (1978) 32–41. `doi:10.1016/0022-3115(78)90026-0`.

[66] D. Carpentier, Simulation of absorption kinetics of point defects by dislocations and defect clusters, Thesis, Université Paris-Saclay (Oct. 2018).
URL `https://pastel.archives-ouvertes.fr/tel-01915303`

[67] S. Kumar, S. K. Kurtz, J. R. Banavar, M. G. Sharma, Properties of a three-dimensional Poisson-Voronoi tesselation: A Monte Carlo study, J. Stat. Phys. 67 (3-4) (1992) 523–551. `doi:10.1007/BF01049719`.
URL `http://link.springer.com/10.1007/BF01049719`

[68] E. A. Lazar, J. K. Mason, R. D. MacPherson, D. J. Srolovitz, Statistical topology of three-dimensional Poisson-Voronoi cells and cell boundary networks, Phys. Rev. E 88 (6) (2013) 063309. `doi:10.1103/PhysRevE.88.063309`.
URL `https://link.aps.org/doi/10.1103/PhysRevE.88.063309`

[69] A. Prokhodtseva, B. Décamps, A. Ramar, R. Schaeublin, Impact of He and Cr on defect accumulation in ion-irradiated ultrahigh-purity Fe(Cr) alloys, Acta Materialia 61 (18) (2013) 6958 – 6971. `doi:http://dx.doi.org/10.1016/j.actamat.2013.08.007`.
URL `http://www.sciencedirect.com/science/article/pii/S1359645413005934`

[70] A. Howie, M. J. Whelan, Diffraction contrast of electron microscope images of crystal lattice defects. III. Results and experimental confirmation of the dynamical theory of dislocation image contrast, Proceedings of the Royal Society of London. Series A. Mathematical and Physical Sciences 267 (1329) (1962) 206–230, publisher: The Royal Society London.

[71] E. Meslin, A. Barbu, L. Boulanger, B. Radiguet, P. Pareige, K. Arakawa, C. C. Fu, Cluster-dynamics modelling of defects in α-iron under cascade damage conditions, J. Nucl. Mater. 382 (2-3) (2008) 190–196. `doi:10.1016/j.jnucmat.2008.08.010`.
URL `http://dx.doi.org/10.1016/j.jnucmat.2008.08.010`

[72] J. F. Ziegler, SRIM-2003, Nuclear Instruments and Methods in Physics Research Section B: Beam Interactions with Materials and Atoms 219-220 (2004) 1027 – 1036. `doi:https://doi.org/10.1016/j.nimb.2004.01.208`.
URL `http://www.sciencedirect.com/science/article/pii/S0168583X04002587`

[73] R. E. Stoller, M. B. Toloczko, G. S. Was, A. G. Certain, S. Dwaraknath, F. A. Garner, On the use of SRIM for computing radiation damage exposure, Nuclear Instruments and Methods in Physics Research Section B: Beam Interactions with Materials and Atoms 310 (2013) 75 – 80. `doi:http://dx.doi.org/10.1016/j.nimb.2013.05.008`.
URL `http://www.sciencedirect.com/science/article/pii/S0168583X13005053`

[74] L. Swartzendruber, V. Itkin, C. Alcock, The Fe-Ni (iron-nickel) system, Journal of phase equilibria 12 (3) (1991) 288–312.

[75] G. F. Bouobda Moladje, L. Thuinet, C. S. Becquart, A. Legris, A phase field model for dislocation climb under irradiation: Formalism and applications to pure bcc iron and ferritic alloys, Int. J. Plast. 134 (2020) 102810. `doi:10.1016/j.ijplas.2020.102810`.
URL `https://doi.org/10.1016/j.ijplas.2020.102810https://linkinghub.elsevier.com/retrieve/pii/S0749641920302126`